DOI: 10.1111/cgf.13445

EuroVis 2018
R. S. Laramee, M. Sedlmair, G. E. Marai
(Guest Editors)

Volume 37 (2018), Number 3
STAR – State of The Art Report

A Survey of Flattening-Based Medical Visualization Techniques

J. Kreiser[1], M. Meuschke[2], G. Mistelbauer[2], B. Preim[2] and T. Ropinski[1]

[1]Visual Computing Group, Ulm University, Germany
[2]Department of Simulation and Graphics, University of Magdeburg, Germany

Abstract

In many areas of medicine, visualization research can help with task simplification, abstraction or complexity reduction. A common visualization approach is to facilitate parameterization techniques which flatten a usually 3D object into a 2D plane. Within this state of the art report (STAR), we review such techniques used in medical visualization and investigate how they can be classified with respect to the handled data and the underlying tasks. Many of these techniques are inspired by mesh parameterization algorithms which help to project a triangulation in $\mathbb{R}^3$ to a simpler domain in $\mathbb{R}^2$. It is often claimed that this makes complex structures easier to understand and compare by humans and machines. Within this STAR we review such flattening techniques which have been developed for the analysis of the following medical entities: the circulation system, the colon, the brain, tumors, and bones. For each of these five application scenarios, we have analyzed the tasks and requirements, and classified the reviewed techniques with respect to a developed coding system. Furthermore, we present guidelines for the future development of flattening techniques in these areas.

Categories and Subject Descriptors (according to ACM CCS): I.3.m [Computer Graphics]: Applied Computing—Life and Medical Sciences

1. Introduction

Medical imaging is one of the corner pillars of medial diagnosis and treatment. By acquiring spatial data sets capturing a patient's or a cohort's characteristics with respect to a certain feature of interest, such features can be analyzed and observed over time. While initially with the advent of computed tomography (CT) only anatomical structures could be imaged, nowadays it is possible to also image a wide variety of functional properties, such as for instance brain activity or metabolism. The growing number of anatomical and functional imaging techniques together with a faster and cheaper acquisition results in a large and ever growing pool of high-resolution medical imaging data, which can be analyzed and taken into account during medical diagnosis. This amount of data enables large scale cohort studies, as for instance the Rotterdam study having acquired medical imaging data of 14,926 subjects since 2008 [HBM*15], but also the detailed observation of a single patient using multiple modalities over time. While there is great potential in this pool of data, it also results in new challenges with respect to its analysis, as multiple data sets have to be taken into account and the high resolution often demands increased inspection times. Furthermore, as the imaged features are inherently 3D, a thorough analysis often requires the inspection from different views.

Classifying flattening techniques. One common approach to deal with the multitude of data made available by nowadays imaging technologies is to exploit parameterization techniques, which allow for mapping 3D data into the 2D plane. Many of these techniques are inspired from computer graphics mesh parameterization techniques, which define a bijective mapping between two triangular surface meshes with the same topology. While these parameterizations are most often used for texture mapping, many other applications exist. The main benefit of these techniques is that they allow for reducing a 2D surface embedded in $\mathbb{R}^3$ down to $\mathbb{R}^2$, and thus make it possible to unfold the object of interest such that it can be mapped onto simpler 2D structures, such as planes. Due to this *projective* nature, these techniques are often referred to as projection-based, and with the result in mind as *flattening* techniques. Due to the expressiveness of the term, we have decided to stick to the later within this state-of-the-art report (STAR). Once a 3D structure is flattened, it can be viewed in its entirety in a single image, which potentially makes complex structures easier to understand by humans and machines. Furthermore, this also facilitates the comparison of data sets, because the 2D projected images can be viewed side-by-side through a juxtaposition or even by overlaying them in a superposition, which are common ways for visual comparisons [GAW*11]. In sum, these techniques have been widely used in medical visualization.

We describe our findings from analyzing the different flattening techniques applied in medical visualization. We divided the surveyed flattening techniques into five groups based on the targeted medical entities: the circulation system, the colon, the brain, tumors, and bones. For each of these entities, we have analyzed

the tasks for which 2D flattenings are used, and describe the main application-specific requirements. Furthermore, we classify the presented techniques through a coding system, which has been derived from the reviewed literature. In particular our coding system has been developed such that it helps readers of this STAR to judge the applicability of a certain technique with respect to a give usage scenario.

One of the most important aspects of the coding system is the *preservation characteristics*. By considering medical tasks we examine two categories, a conformal one which preserves angles, and an equiareal one, preserving area while mapping from the object's surface to its corresponding parameter domain. Combining these two characteristics creates an isometric parameterization, preserving lengths while mapping from one space to another. In case the parameterization underlying a flattening technique is isometric, the flattening preserves the geodesic distance between any pair of points on the surface. Thus, measurements can be performed in the flattened representation, which is important when performing quantification within a medical diagnosis step. Within this STAR we analyze these and other properties with respect to the reviewed techniques. Finally, for each application area, we provide usage guidelines, which we have derived from the reviewed papers. These guidelines have been developed in order to support researchers when developing new medical projection techniques.

Related surveys. During the time of writing of this STAR, a few related survey papers exist. Many of these surveys are published in computer graphics venues and focus on mesh parameterizations [FH02, FH05, SPR06, LI15]. None of them directly targets medical applications or visualization, and their rather technical nature makes it difficult for domain experts to distill which projection techniques are useful for a given data set or medical task.

Other surveys are more related to this STAR. Toga et al. provide a, rather outdated, survey of brain mapping techniques [TT99]. Bühler et al. [BFLC04] present a survey about geometric models for vessel visualization. However, they focus in their work mainly on skeletonization, deformable models, and iso-surface extraction, vessel flattening is only briefly discussed. Saroul reviews some flattening techniques for anatomical visualization in his Phd thesis [Sar06], but does neither provide the breadth nor the classification offered within this STAR. In these surveys, many newer important techniques are not covered. One first step in this direction has been taken in an online chapter, which was released in 2013 as an appendix to the book by Preim and Botha [PB13]. In the chapter on *Projections and Reformations* around 20 such techniques are discussed. Despite a similar topic is discussed, there are at least two major differences between this chapter and our STAR. First, the chapter only discusses a small subset of the available techniques, even with respect to the literature available in 2013. Second, while we have developed an elaborate coding system, which helps to put the available techniques into context, the chapter only groups them into three types: anatomical unfolding, anatomical planar reformation and projection, and map projection techniques. This rather technical differentiation does not take into account preservation characteristics relevant for a quantitative diagnosis. Furthermore, delineating types based on the technology does not help to find the right technique for the medical use case at hand.

Software solutions. Due to the importance of flattening techniques in the medical field, in the past years several software systems have been released, which help users to perform flattening on their data. While describing these systems would be beyond the scope of this STAR, we provide links to them, such that the interested reader is able to explore some of the techniques discussed in this STAR. When examining the software available, several systems dedicated to brain analysis emerge, e.g., FreeSurfer [Fis12] and BrainSuite [SL02]. The SureFit system [VEDD*01] provides general surface reconstruction through intensity filtering and transformations. The Computerized Anatomical Reconstruction and Editing Tool Kit (CARET) [VEDD*01] provides surface visualization, but also analysis possibilities which are based on flattening. Other systems solving similar tasks, but on an even more general level, are CirclePack [HSS*99], Hip-Hop [ALLT*13], and SurfRelax [Lar01]. While this list of software systems is not complete, it gives the reader some starting pointers.

Literature under review. When selecting the literature for this report, we have chosen the initial papers from each field of application and then proceeded with the state of the art. We did not exclusively choose any conference of journal, as there are contributions from computer science, mainly graphics and visualization, and the medical field. The main criteria was that the topic of projection or flattening has to be covered in a medical context to provide a good overview for fast visual analysis in 2D rather than 3D. Either if a parameterization technique itself was developed or used for visualization purposes. Furthermore, we did not take the number of citations per paper into account to not exclude the most recent work.

Outline. This report is structured as follows. We will introduce a coding system in Section 2. The reviewed techniques are then discussed in Section 3 to Section 7. Each of these sections focuses on one specific application area. All these sections follow the same structure: First, the application-specific tasks and requirements are discussed, before the reviewed techniques are classified with respect to the proposed coding system. After describing the reviewed techniques, we discuss general usage guidelines for medical projections in Section 8. The STAR concludes with a brief summary in Section 9 and Future Challenges in Section 10.

2. Coding System

To put the reviewed techniques into context, we have developed a multi-dimensional coding system which takes into account seven axes for each flattening technique. The system has been developed based on the reviewed literature and the benefits and downsides we could identify in each reviewed publication. The seven classification axes have been divided into three groups. These groups are labeled *Input Data*, *Transferability*, and *Preservation*. Figure 1 gives ans overview of the taxonomy we use in this paper.

Our coding system is tailored for two use cases. First, users are supported when choosing an approach suitable for their individual problem. Second, developers of new algorithms can identify which properties can still be improved and which are already sufficiently implemented and well established in each field of application. This allows to gain a quick overview of those properties relevant to each application. When sorting new techniques into the coding system, a direct comparison of its capabilities is possible.

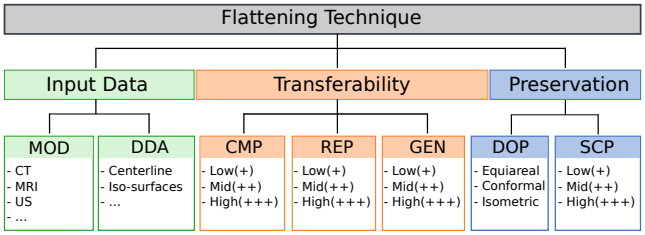

Figure 1: *This taxonomy graph describes our coding system with its three classification groups and characteristics.*

In each of the five individual application sections, the approaches are sorted in a chronological order and put into relation where possible. The methods' corresponding classification properties are rated and presented in Table 1 with a matching color scheme of each group according to Figure 1. Below we will outline the identified classification axis within these three groups.

Input Data. Our first group is focused on the data to be flattened. It contains two axes which take into account data modality and the requirements with respect to the derived data. For the Data Acquisition Modality (**MOD**), we specify the data source for which a certain flattening technique has originally been developed. We denote this axis by specifying different labels, such as US for ultrasound, CT for computed tomography, MRI for magnetic resonance imaging, PET for positron emission tomography. While this property specifies the modalities that a technique has originally been developed for, it does not mean that the technique could not be transferred to other modalities. Besides the modality, we consider which Derived Data Attributes (**DDA**) are required by a certain flattening technique. Many of the reviewed flattening techniques require the derivation of such data, e.g., isosurfaces or centerlines. As it is not possible to derive such attributes in all cases robustly, we feel that this is an informative property for flattening applications.

Transferability. The second group is targeted towards the transferability of a certain technique. Some flattening techniques can be transferred to different structures, i.e., organs, some only to similar structures, and some might not be applicable to other structures at all. To describe this situation adequately, we have identified three properties within this group. Comparability (**CMP**) describes if a flattening technique can be used to compare several instances of the same subject or across different subjects. Here, we distinguish between intra- **(A-CMP)** and inter-subject **(E-CMP)** comparability. CMP is directly related to Reproducibility (**REP**), which specifies the applicability of the projection for many instances of the *same* organ. We would like to point out that it can be seen as a measure of the projection's stability across many data sets. Finally, Generalizability (**GEN**) specifies the applicability of the projection to a multitude of *different* organs. Thus, if a technique has been developed for instance for the brain, we specify if it is transferable to other organs, such as the heart. CMP, REP, and GEN are classified as Low (+), Mid (++), or High (+++). For CMP, we provide a separate classification for intra- (A-CMP) and inter-subject (E-CMP) comparability.

Preservation. Within the second group of coding axes, we focus on preservation properties. Here, we have identified two axes. Degree of Preservation (**DOP**) is targeted towards a quantitative analysis and thus reviews the type of the projection preservation. Instances of this property are Equiareal, Conformal, and/or Isometry for an area, angle, and/or length preserving flattening, respectively. If one of these properties applies only partially, we denote it with the prefix *quasi*. As outlined in the introduction, we consider this property as critical for all diagnosis and comparison-related tasks. Besides the actual structures under investigation, it is also important to realize Spatial Context Preservation (**SCP**), which helps users to contextualize the observed structures. This is especially important if large deformations occur. The better the spatial context is preserved, the easier a certain region can be mentally mapped to its corresponding position in the original data. We provide the following values for this property: Low (+), Mid (++), High (+++).

3. Application: Circulation System

Cardiovascular diseases (CVDs) are the world's leading cause of death. Their initiation and progression depend strongly on factors such as genetics, inflammation, morphological conditions, and internal blood flow. However, the interplay of these factors is not well understood. Thus, medical researchers investigate morphological and hemodynamic information, which can be quite challenging due to the complexity of the data. Flattening techniques are commonly used to support clinical physicians and medical researchers in analyzing CVDs.

3.1. Tasks and Requirements

Medical researchers are interested in better understanding the causes of the evolution of CVDs. They analyze how flow patterns and scalar flow parameters are changing over the cardiac cycle to detect suspicious parameter correlations. There already exist a lot of advanced visualization techniques that support the exploration of medical flow data [OJMN*18]. Many of these approaches are based on 3D visualizations. However, due to the complexity of medical flow data, such visualizations are affected by visual clutter and occlusions. Moreover, a series of manual rotations is necessary to gain a complete overview, because only the currently visible surface parts can be investigated. To overcome these limitations, flattening techniques are often used to generate occlusion-free visualizations of the vessel anatomy. With respect to the exploration of aneurysm data, such mappings should present the aneurysm sac as well as quantitative flow characteristics, i.e., color-coded on the 2D structure. To support aneurysm treatment decisions, the mapping should also preserve the anatomy of the parent vessel geometry to observe the influence of different treatment configurations. According to the myocardium, the mapping should present different anatomical regions of the myocardium as well as quantitative and qualitative flow features.

Due to the time-dependent behavior of simulated or measured flow data, a major task is to observe flow characteristics in different time steps along the cardiac cycle. For this purpose, side-by-side visualizations could be used. However, only a small amount of time steps or parameters could be analyzed simultaneously and it is quite

Table 1: *Application-specific literature classified according to our coding system in Figure 1 with matching color scheme for each group. The degree of preservation (DOP) comprises conformal (con), isometric (iso), quasi-conformal (q-con), quasi-isometric (q-iso), equiareal (eq-a).*

			Input Data		Transferability				Preservation	
Application	**Year**	**Authors**	**MOD**	**DDA**	**A-CMP**	**E-CMP**	**REP**	**GEN**	**DOP**	**SCP**
Circ. Sys.	2001	He et al. [HDL*01]	CTA	centerline	+	+	+++	+	q-iso	++
Circ. Sys.	2002	Kanitsar et al. [KFW*02] (projected)	CTA	centerline	++	+	+	+	none	+++
Circ. Sys.	2002	Kanitsar et al. [KFW*02] (stretched)	CTA	centerline	++	+	++	+	q-iso	++
Circ. Sys.	2002	Kanitsar et al. [KFW*02] (straightened)	CTA	centerline	++	+	+++	+	q-iso	+
Circ. Sys.	2002	Cerqueira et al. [CWD*02]	MRI	none	++	++	+	+	none	+
Circ. Sys.	2002	Zhu et al. [ZHT*02a]	MRA, CT	centerline, radius, mesh	+	+	++	+	con	+
Circ. Sys.	2002	Zhu et al. [ZHT02b]	MRA, CT	centerline, radius, mesh	+	+	++	+	con	+
Circ. Sys.	2003	Kanitsar et al. [KWFG03]	CTA	centerline, vessel tree	++	+	++	+	q-iso	+
Circ. Sys.	2003	Kanitsar et al. [KWFG03]	CTA	centerline, vessel tree	++	+	++	+	q-iso	++
Circ. Sys.	2003	Zhu et al. [ZHT03]	MRA, CT	centerline, radius, mesh	++	+	++	+	con, eq-a	++
Circ. Sys.	2005	Zhu et al. [ZHT05]	MRA, CT	centerline, radius, mesh	++	+	++	+	con, eq-a	++
Circ. Sys.	2006	Lee and Rasch [LR06]	CTA	centerline	++	+	++	+	none	+
Circ. Sys.	2006	Oeltze et al. [OGH*06]	MRI, CTA	mesh	++	++	+++	+	none	+
Circ. Sys.	2007	Termeer et al. [TBB*07]	MRI	centerline, contours, mesh	++	++	+++	+	none	++
Circ. Sys.	2007	Cai [Cai07]	CTA	centerline, radius	++	+	+++	+	none	+
Circ. Sys.	2008	Chiu et al. [CES*08]	Ultrasound	mesh, centerline	+++	+	++	+	q-iso, eq-a	++
Circ. Sys.	2008	Lv et al. [LGZ08]	CTA	centerline	+	+	+++	+	con	+
Circ. Sys.	2009	Lampe et al. [LCMH09]	seismic, car wind sim.	centerline	+	+	+++	+	con	+
Circ. Sys.	2009	Neugebauer et al. [NGB*09]	MRA	mesh	++	+	++	++	none	+
Circ. Sys.	2010	Markl et al. [MBS*10]	4D PC-MRI, 3D GRE	mesh	++	++	+++	++	none	++
Circ. Sys.	2011	Angelelli and Hauser [AH11]	PC-MRI, exhaust sys.	centerline, flow field	+	+	+++	+	con	++
Circ. Sys.	2011	Borkin et al. [BGP*11]	CTA, ESS	centerline, wall shear stress	+	+	+++	+	none	+
Circ. Sys.	2012	Mistelbauer et al. [MVB*12]	CTA	centerline	++	+	++	+	none	+++
Circ. Sys.	2012	Goubergrits et al. [GSK*12]	MRA, CTA	mesh	++	+	++	++	con	+
Circ. Sys.	2013	Auzinger & Mistelbauer et al. [AMB*13]	CTA	centerline	++	+	+++	+	none	+++
Circ. Sys.	2013	Diepenbrock et al. [DHS*13]	PET/CT	centerline, wall thickness, radius	+	+	+++	+	none	+
Circ. Sys.	2013	Mistelbauer et al. [MMV*13]	CTA	centerline	+	+	+++	+	none	+
Circ. Sys.	2015	Köhler et al. [KMP*15]	MRI, 4D PC-MRI	centerline, mesh	++	++	+++	++	none	+
Circ. Sys.	2016	Sheharyar et al. [SCK*16]	MRI, TPM	segmentation	++	++	+++	+	none	+
Circ. Sys.	2016	Meuschke et al. [MKP*16]	MRI, 4D PC-MRI	centerline, mesh	++	++	+++	++	none	+
Circ. Sys.	2016	Tao et al. [THQ*16]	MRA, CTA	mesh	++	+	++	++	con	+
Circ. Sys.	2016	Cui et al. [CWW*16]	CTA	centerline, cross-sec. radius/area	+	+	+++	+	con	+
Circ. Sys.	2016	Marino and Kaufman [MK16]	NA	centerline, radius	+++	+	+++	+	q-con	+++
Circ. Sys.	2017	Meuschke et al. [MVB*17]	MRA, CTA	mesh	++	+	++	++	con	++
Circ. Sys.	2017	Miao et al. [MMK*17]	MRI	segmentation	+	+	+++	+++	con	+
Colon	2000	Haker et al. [HATK00a]	CT	mesh	++	++	+++	++	con	++
Colon	2000	Haker et al. [HATK00b]	CT	mesh	++	++	+++	++	con	++
Colon	2001	Bartrolí et al. [BWKG01]	CT	centerline	+	+	+++	+	eq-a	+
Colon	2005	Lee et al. [LLS05]	MRI, CT	centerline, radius	++	++	++	+	none	+
Colon	2006	Hong et al. [HQG*06]	CT	mesh, centerline	++	++	+++	++	con	+
Colon	2007	Mai et al. [MHS07]	CT	mesh, centerline	+	+	++	+	none	+
Colon	2008	Williams et al. [WGC*08b] (projected)	CT	centerline	++	++	+++	+	none	+++
Colon	2008	Williams et al. [WGC*08b] (stretched)	CT	centerline	++	++	+++	+	q-iso, con	++
Colon	2008	Williams et al. [WGC*08b] (straightened)	CT	centerline	++	++	+++	+	q-iso, con	+
Colon	2010	Zeng et al. [ZMG*10]	CT	mesh, centerline	+++	++	++	++	q-con	+
Colon	2010	Zeng et al. [ZMGK10]	CT	mesh, centerline	+++	++	++	++	con	+
Colon	2011	Zeng et al. [ZMKG11]	CT	tetrahedral mesh	+	+	+++	++	con	+
Colon	2011	Marino et al. [MDB*11]	MRI, CT	centerline, radius	+	+	+++	+	con	+
Colon	2013	Gurijala et al. [GSZ*13]	CT	none	+++	++	+++	+++	q-con	++
Colon	2014	Lu and Zhao [LZ14]	CT	inner/outer mesh, centerline	+	+	+++	+	q-con	++
Colon	2017	Nadeem et al. [NMGK17]	CT	mesh, centerline	+++	++	+++	++	q-con	++
Brain	1999	Angenent et al. [AHTK99a]	MRI	mesh	+	+	+++	+	con	+
Brain	1999	Angenent et al. [AHTK99b]	MRI	mesh	+	+	+++	+	con	+
Brain	1999	Timsari [Tim99]	MRI	mesh	++	++	+++	++	q-iso	+
Brain	1999	Hurdal et al. [HBS*99]	MRI	mesh, landmark curves	++	++	++	++	q-con	+
Brain	2000	Goebel [Goe00]	MRI	mesh	+	+	++	+	q-iso	+
Brain	2000	Timsari and Leahy [TL00]	MRI	mesh	++	++	+++	++	q-iso	+
Brain	2000	Wandell et al. [WCB00]	MRI	mesh	+	+	+++	++	q-iso	+
Brain	2001	Tosun and Prince [TP01]	MRI	mesh, crest lines	+++	+++	+++	+	con, eq-a	++
Brain	2004	Gu et al. [GWC*04]	MRI	mesh, landmark curves	+++	+++	+++	+	con	++
Brain	2004	Hurdal and Stephenson [HS04]	MRI	mesh, landmark curves	++	++	++	++	con	+
Brain	2004	Joshi et al. [JSTL04]	MRI	mesh, inter-hemispheric fissure	++	++	+++	+	con	+
Brain	2004	Ju et al. [JSR*04]	MRI	mesh	+	+	+++	++	q-con	+
Brain	2004	Pons et al. [PKF04]	MRI	mesh	++	++	+++	++	eq-a	+++
Brain	2004	Stylianou and Farin [SF04]	MRI	mesh, crest lines	+	+	+++	+	eq-a	+
Brain	2004	Tosun et al. [TRH*04]	MRI	mesh, crest lines	+++	+++	+++	+	con, eq-a	++
Brain	2004	Tosun et al. [TRP04]	MRI	mesh, crest lines	+++	+++	+++	+	con, eq-a	++
Brain	2004	Wang et al. [WGC*04a]	MRI	mesh, landmark curves	++	++	+++	++	con	++
Brain	2004	Wang et al. [WGC*04b]	MRI	tetrahedral mesh	+	+	+++	++	con	+
Brain	2006	Memoli et al. [MST06]	MRI	mesh, landmark curves	+++	+++	+++	++	q-iso	+
Brain	2008	Kwon et al. [KHP08]	MRI, MPRAGE	mesh	+	+	+++	+	q-iso	+
Brain	2008	Wang et al. [WGC*08a]	MRI	mesh, landmark curves	+++	+++	++	++	con	++
Brain	2009	Hurdal and Stephenson [HS09]	MRI	mesh, landmark curves	++	++	++	++	con	+
Brain	2010	Balasubramanian et al. [BPS10]	MRI, PET	mesh	+++	+++	++	+++	q-iso	+
Brain	2010	Lui et al. [LTW*10]	MRI	mesh, landmark curves	++	++	++	++	con	++
Brain	2011	Zou et al. [ZHGH11]	MRI	mesh	+	+	+++	+++	eq-a	+
Brain	2012	Wang et al. [WSY*12]	MRI	mesh, landmark curves	+++	+++	+++	+++	con	++
Brain	2013	Su et al. [SZS*13]	MRI	mesh	++	++	++	++	eq-a	+
Brain	2013	Auzias et al. [ALLT*13]	MRI	mesh, landmark curves	+++	+++	+++	+	con	++
Brain	2014	Khosravi and Soltanian-Zadeh [KSZ14]	MRI	multi-surface mesh	++	++	++	+	q-iso	+
Brain	2015	Choi et al. [CLL15]	MRI	mesh, landmark curves	+++	+++	+++	+	con	++
Tumor	2010	Rieder et al. [RWS*10]	MRI	segmentation	+	+	++	++	none	+
Tumor	2010	Diepenbrock et al. [DPL*10]	MRI	segmentation	+	+	++	++	none	++
Bone	2005	Vrtovec et al. [VLP05]	CT	centerline	+	+	+++	+	none, con	++
Bone	2006	Vrtovec et al. [VOG*06]	CT	centerline	+	+	+++	+	none, con	++
Bone	2006	Saroul [Sar06]	CT	segmentation, central surface	+++	+++	+++	+++	eq-a	+
Bone	2007	Vrtovec et al. [VOG*07]	CT	centerline	+	+	+++	+	none, con	++
Bone	2010	Kok et al. [KBH*10]	CT	segmentation, central surface	+++	+++	+++	+++	eq-a	+
Bone	2010	Ringl et al. [RSS*10]	CT	segmentation	+++	+++	+	+	none	+
Bone	2012	Coffey et al. [CKHS*12]	CT	none	++	++	+++	++	q-iso	+++
Bone	2013	Klemm et al. [KLR*13]	CT	none	+++	+++	+++	+	eq-a	+
Bone	2014	Kretschmer et al. [KST*14]	none	defined surface	++	++	+++	+++	con, q-iso	+++
Bone	2015	Vrtovec [VOG*07]	CT	centerline	+	+	+++	+	none, con	++
Bone	2015	Ringl et al. [RLT*15]	CT	none	+++	+++	++	+	q-iso	+++
Bone	2017	De Leener et al. [DMD*17]	MRI	centerline	+++	+++	+++	+	con	+++
Bone	2017	Martinke et al. [MPG*17]	CT	centerline, radius, cross-section	+++	+++	+++	+	con	++

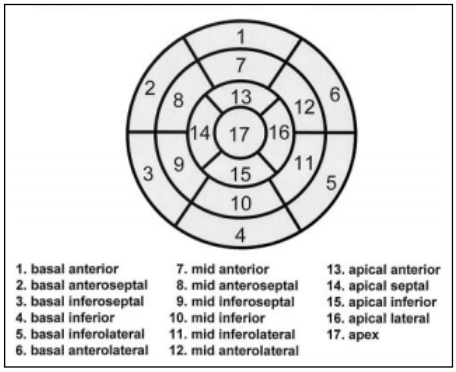

Figure 2: *Segments of the Cardiac Bull's Eye Plot. The myocardium is mapped on a circumferential polar plot, consisting of 17 segments. (From [CWD*02])*

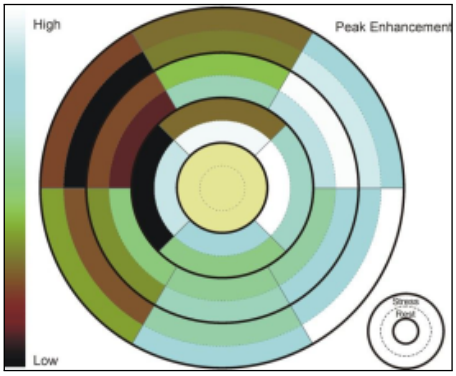

Figure 3: *Visualization of rest and stress perfusion using a refined BEP. Each ring represents an ischemic area from anterior to inferoseptal along the septum. Dark regions indicate a diminished perfusion. Segment 17 (yellow area) is missing since no slice has been acquired at the apex itself. (From [OGH*06])*

difficult for the medical expert to mentally combine these multiple images. Thus, mapping techniques are used to depict spatio-temporal features in a more dense visualization. Important qualitative features are vortices related to pathogenesis. The flattening of the respective vasculature should depict where and at which point in time such flow patterns occur.

Besides exploration of an individual data set, comparing healthy and pathological data sets is essential to improve diagnosis and treatment planning. Similar to the observation task, side-by-side views are used for comparison in medical research literature. Due to the limitations of 3D visualizations, flattening techniques are also used for comparing data before and after treatment, among different treatment scenarios, and across patients. Similar to the previous tasks, it is important to depict scalar and vectorial blood flow information as well as the vessel morphology. Moreover, interesting regions, i.e., according to user-selected scalar fields should be highlighted. In the following section we will describe flattening techniques, developed in the context of the circulation system.

3.2. Techniques

Within this subsection, we review flattening techniques related to the circulation system. Thus, we will discuss myocard flattening in Section 3.2.1, aneurysm maps in Section 3.2.2, vessel fattening in Section 3.2.3, and placenta maps in Section 3.2.4.

3.2.1. Myocard Flattening

The Cardiac Bull's Eye Plot (BEP) is very popular and a basis for many plots related to cardiac imaging. It is based on a standard segmentation of the myocardium [CWD*02]. Parts of the heart wall are projected onto 17 planar segments, arranged circularly, see Figure 2. This results in an anatomical unfolding of the conical heart wall, where the cardiac apex is mapped to the center of the plot. With the help of the BEP, it is possible to reduce complex 3D data to a simple 2D visualization. Cardiologists are trained with this segment division worldwide, so that they can immediately interpret the presented information and mentally reconstruct the original geometry.

Oeltze et al. [OGH*06] use the BEP to display perfusion data that is relevant for the diagnosis of coronary heart disease, see Figure 3. Perfusion data is often acquired at rest and under stress, induced by specific medicines. For the simultaneous representation of rest and stress perfusion, the number of segments is doubled along the rings of the plot, resulting in 34 segments. This ring-wise subdivision of the segments ensures that adjacent segments in the plot are adjacent to the heart wall. In this way, the influence of rest and stress on the perfusion in the respective area can be visualized.

The standard BEP exhibits some limitations. First, the segments give a quantized view of the data and do not display the amount of scar tissue and its distribution simultaneously. Moreover, the BEP does not provide any anatomical information. To overcome these disadvantages, Teermeer et al. [TBB*07] introduce the volumetric BEP (VBEP), see Figure 4. Similar to the BEB, the shape of the ventricle is mapped to a cone which is unfolded onto a plane. However, to construct the VBEP, the thickness of the heart wall has to be mapped to the thickness of the cylinder. This removes discontinuities in the representation of the data and the resulting volume preserves the amount and position of scar tissue. Furthermore, anatomical information is added to the VBEP by projecting the coronary arteries and displaying two dots representing the locations where the right ventricle joins the left ventricle.

Sheharyar et al. [SCK*16] provide novel visualization techniques to analyze regional motion patterns of the myocardium using the BEP. With this technique, abnormal motion of myocardium can be detected, which is an important indicator for multiple cardiac pathologies. They used two coordinated views for navigating through the spatio-temporal domain. The first view consists of three arranged plots that visualize the myocardial motion over the cardiac cycle at three slices along the left ventricle. For this purpose, the temporal component of motion is mapped to the plot's radius, and its anatomical location is mapped to the plot's angle. The second view allows for a more detailed exploration of an individual time step, in which motion is depicted based on the segments of the BEP. For visual encoding of the myocardial motion, different tech-

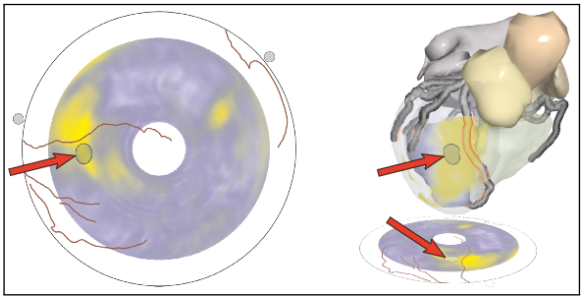

Figure 4: *The left image shows a VBEP with a global cursor (indicated with the red arrow) highlighting scar tissue of the myocardium. The same region is highlighted in an anatomical view, presented in the right image. (From [TBB*07])*

niques are provided, i.e., warped BEP segments, pins, and warped lines, where a blue-to-red color scale is used to depict the motion strength for all designs. These techniques are inspired by the work of Föll et al. [FJS*09], who visualized myocardial motion with arrow glyphs on the BEP.

Markl et al. [MBS*10] present a 2D plot representation which transfers the segment-wise subdivision of the BEP to the aorta, see Figure 5. The aim is to investigate correlations between plaques and forces acting on the vessel wall, such as the Wall Shear Stress (WSS). For this purpose a study with 94 patients was performed, where 144 plaques thicker than 4 mm were localized within the aorta. For the exploration of the wall forces, eight planes, intersecting the vessel surface, are calculated. Each intersecting plane is subdivided into 12 segments and each segment is colored according to the WSS by using a dark blue-to-white color map. All segments of all intersecting planes are arranged in a circle. Yellow markings indicate critical aortic areas with respect to the wall forces and at the same time they facilitate the orientation. Furthermore, the number of plaques was color-coded for each segment to find suspicious regions.

Köhler et al. [KMP*15] have developed a circular plot, called *Aortic Vortex Plot* (AVP), based on the BEP to represent vortical blood flow in the aorta, see Figure 6. The aim is to enable an efficient analysis of aortic vortices that are presumed to be a strong indication of several cardiovascular diseases. The AVP provides detailed information about the spatial and temporal position of vortex flow and avoids the visual clutter of a path line-based flow representation. For the mapping of the vortex flow, representing path lines, the radius and angle of the AVP is used. The temporal position of each path line point is mapped to the angle. Its corresponding aortic section is mapped to the radius.

Meuschke et al. [MKP*16] extend the approach by Köhler et al. [KMP*15] to analyze the spatial-temporal behavior of aortic vortex entities over the cardiac cycle. They restrict the number of radial segments to four based on an anatomically motivated subdivision and color-code predetermined vortex entities over time. Therefore, path lines representing aortic vortex flow are clustered to obtain vortex entities. For each path line point the corresponding plot segment is calculated. It is colored according to the pre-defined

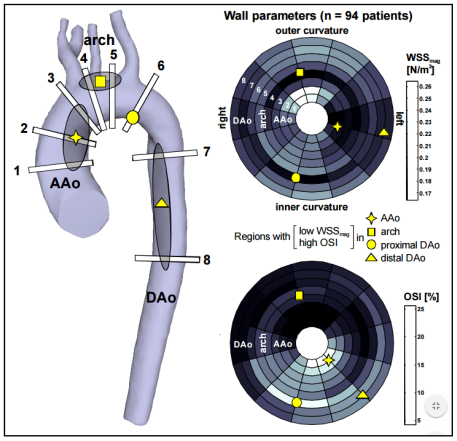

Figure 5: *Map-based analysis of correlations between plaques and the Wall Shear Stress in the ascending aorta. The aortic map contains 12 segments along the vessel circumference and is constructed using eight cutting planes. The color-coding represents the averaged distribution of the mean WSS and OSI per segment. (From [MBS*10])*

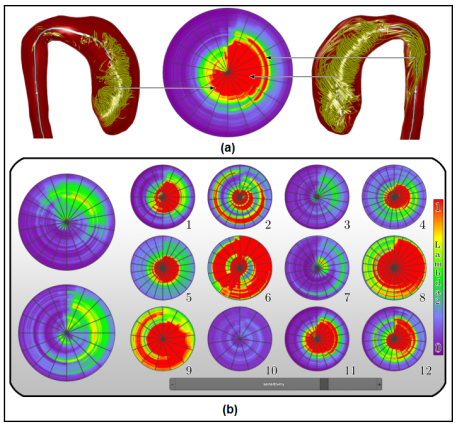

Figure 6: *Grid-based view of different AVPs. In (a), diastolic (left) and systolic vortex flow (right) of a patient with an aortic ectasia is depicted. In (b), two larger AVPs of probands are presented on the left side as a reference, and on the right side three more probands (3,7,10) as well as two patients with an ectasia (1,11) and seven patients with a bicuspid aortic valve are illustrated. (From [KMP*15])*

vortex color. For the mapping of the path line points the approach by Köhler et al. [KMP*15] has been used.

3.2.2. Aneurysm Maps

Cerebral aneurysms are widenings of cerebral arteries that bear a risk of rupture. They often have an irregular and complex shape that complicates their analysis. A visual inspection of the aneurysm wall and associated wall parameters in 3D requires interaction and a mental integration of currently visible and hidden surface parts.

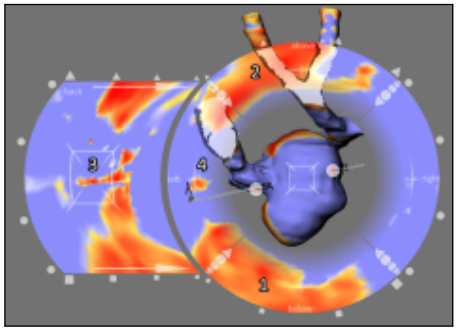

Figure 7: *Map projection of a cerebral aneurysm. In the center, the colored 3D vascular surface is depicted surrounded by a five-part map showing the flow information of the left, right, upper, lower, and retral sides of the aneurysm surface. (From [NGB*09])*

Thus, several publications discuss the generation of more abstract representations such as a sphere or a 2D map.

A simple visualization of scalar flow information is to color-code the scalar values on the three-dimensional vessel surface. However, not all areas of the surface can be analyzed at the same time. Neugebauer et al. [NGB*09] present a map that projects scalar flow data of cerebral aneurysms. This is combined with a 3D view of the geometry to establish a relation between both views. In the center of the illustration, the colored 3D vascular surface is shown, surrounded by the map, see Figure 7. The map consists of five regions, which represent the flow information of the left, right, upper, lower and back sides of the vessel surface. Outgoing vessels obscuring the map are displayed semi-transparently. A bi-directional interaction between the two views allows fast and easy navigation and analysis of the data.

Goubergrits et al. [GSK*12] transform the aneurysm surface to a uniform spherical shape to analyze statistical WSS distributions. Therefore, the vertices of the aneurysm surface are transformed towards the center of mass of the aneurysm, where they ensured that the distance to the center is equal for all vertices. The sphere is then mapped to a disc using an azimuthal equidistant projection. For convex structures, where the center of mass lies inside the surface, this approach produces reasonable results. However, for more irregularly shaped aneurysms, where the center of mass is located outside the surface, this method leads to area distortions of the calculated disc representation which increases for regions more distant to the map's center (aneurysm dome).

Tao et al. [THQ*16] present the *VesselMap*, a 2D visualization of a cerebral aneurysm and parent vasculature, see Figure 8. The view-dependent mapping is formulated as a 2D graph layout optimization problem. Small spatial partitions of the vasculature in 3D are considered as nodes that must not overlap in 2D while at the same time spatial relations must be preserved. The result exhibits rather strong local distortions but the overall vascular topology is maintained. The VesselMap is integrated in an interactive visual analysis framework and serves as a fast interaction with the associated hemodynamic data, e.g., by brushing interesting spatial regions.

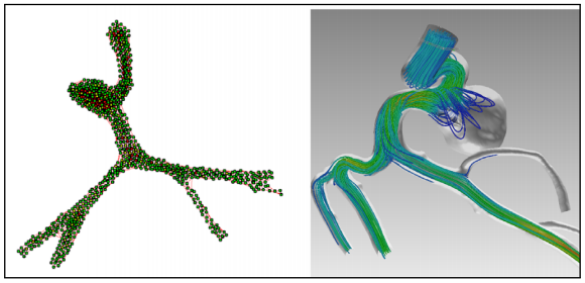

Figure 8: *Mapping from the 3D volume space to a 2D VesselMap representation. (a) shows the mesh structure of the VesselMap. (b) shows streamline visualization with a semi-transparent vessel structure. (From [THQ*16])*

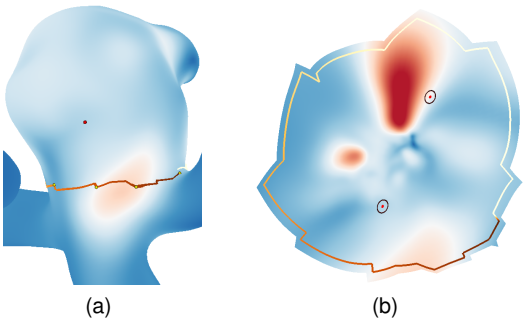

Figure 9: *For the 2D map generation, the user defines markers along the aneurysm ostium that are connected to a cut line and two markers on the dome (one is depicted as red point) (a). The surface is unfolded where the dome markers and the ostium were emphasized in the map (b).*

Meuschke et al. [MVB*17] use the *least squares conformal maps* technique [LPRM02] to parameterize the aneurysm surface, see Figure 9. They generated a 2D aneurysm map that provides an occlusion-free overview visualization. The map correctly depicts angles but suffers from area distortions. It requires a user-defined delineation of the aneurysm ostium along which the surface is cut off as well as the definition of two landmarks for parameterization. The map can be colored according to one hemodynamic or morphological parameter and hatched according to a second. This allows a simultaneous analysis of two scalar fields to identify possible rupture-prone correlations. The map is bidirectionally linked to a 3D view of the aneurysm showing the same encoding.

3.2.3. Vessel Flattening

Achenbach et al. [AMRB98] introduce curved multiplanar reconstructions to inspect the interior of blood vessels along a curve. This approach builds the foundations for curved planar reformation (CPR). Kanitsar et al. [KFW*02, Kan04] distinguish between three types of curved planar reformation (CPR), depending on the way the centerline is projected or flattened into the image space, as illustrated in Figure 11. One important aspect is that CPRs are not only characterized by a curved cut through a blood vessel along

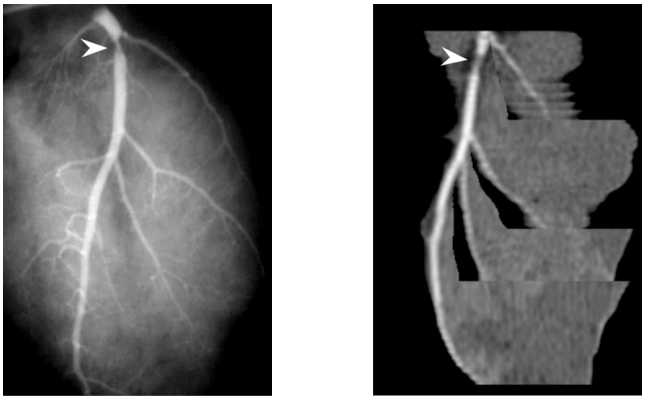

Figure 10: *A stenosis (white arrows) of a postmortem pig heart. (a) shows the common angiogram, whereas (b) demonstrates the MAR that clearly represents the stenosis. (From [HDL*01])*

its centerline to visualize the vessel lumen. It also provides a cut through the surrounding parts of the vessel as well. This is considered useful, as possible other diseases could be spotted during the assessment of the vessel. As the vascular system usually consists of more than one vessel, inspecting each separately using CPR is a time-consuming task. Therefore, a **multi-path curved planar reformation (mpCPR)** can be assembled out of the individual CPRs by means of image partitioning [KFW*02, Kan04, KFWG06]. Subsequently, we explain each type of CPR in detail.

He et al. [HDL*01] propose **medial axis reformation (MAR)**, a technique for creating curved cuts along the medial axis or centerline of a blood vessel to inspect its interior for potential pathologies such as stenoses. Their approach firstly partitions a single vessel into slabs or regions of interest (RoI) along the centerline and computes the centroids of each of these slabs. Secondly, the multiscale medialness is computed within every slab in order to re-center the centroids. The curve spanned by these points defines the refined centerline used to generate the curved reformation. In the last and third step, the MAR presents the lumen of several vessels simultaneously in one image in their full length, resembling a stretched mpCPR with correct visibility and preserved isometry. An example of MAR is presented in Figure 10.

Kanitsar et al. [KWF*01] present a tool for semi-automatic segmentation of blood vessels and bones in peripheral computed tomography angiography (CTA) datasets in order to generate CPRs of vasculature of the human lower extremities. They describe an approach to determine a vessel centerline between two user-specified points using a cost function and Dijkstra's shortest path algorithm.

The **projected** CPR (see Figure 11) projects the centerline into the image space using a parallel projection, resulting in the loss of isometry and conformity [KFW*02]. By resampling the volumetric input data along the centerline of a blood vessel, the CPR surface is generated. It is a ruled surface, defined by a so-called *vector of interest* that sweeps along the centerline and is either coplanar with the *xy*-plane (transverse or axial slice) or perpendicular to the centerline. In the latter case, large blood vessels' radii could lead to artifacts due to overlapping vectors of interest. The advantage of the projected CPR is the well preserved spatial contextual relation. It is clearly visible, where the currently inspected blood vessel is located in the acquired dataset. Nevertheless, due to the perspective occlusion of the projection, several images have to be generated in order to inspect the lumen of a blood vessel in its entirety. This technique has been extended to support multiple paths or branches of a vascular system at once in a single image. This is achieved by partitioning the image space at the position of the projected branching points horizontally as well as vertically [KFWG06]. By rotating the vector of interest around a predefined axis (commonly the *z*-axis) or the centerline, CPR images around the entire vessel lumen are generated, allowing the assessment of the vessel lumen for possible stenosis.

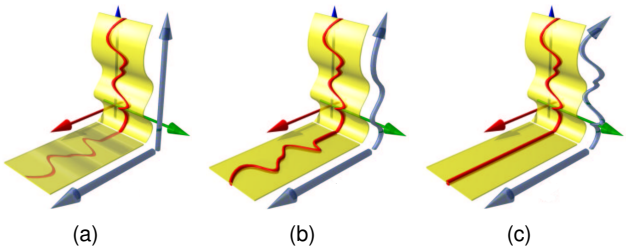

Figure 11: *Different types of CPRs. The centerline of the vessel is depicted in red and the cut surface in yellow. The vertically oriented surface presents the surface within the data set, whereas the horizontal one the corresponding projected or flattened one. (a) resembles the projected CPR, (b) the stretched, and (c) the straightened. (From [KFW*02])*

Locally straightening the centerline of a blood vessel when projecting it into the image space preserves isometry, if the vector of interest is coplanar to the *xy*-plane, and is referred to as **stretched** CPR (see Figure 11). If the surface is generated by a vector of interest that is perpendicular to the centerline, isometry will not be preserved. Furthermore, this provides an unobstructed view of the blood vessel lumen while still retaining a good overall spatial context relation. By projecting equidistant samples along the centerline into the image plane, depending on the orientation of the vector of interest and line of interest (the direction of the centerline), each sample is projected to a single row in the final image. Extending this method to visualize the lumen of multiple vessels is possible, but the spatial coherence and relation might be further reduced due to the different stretching factors of different vessel branches. Analogously to the projected CPR, by rotating around a predefined axis (commonly the *z*-axis), several stretched CPRs allow an obstruction-free and simultaneous assessment of multiple vessel lumina at specific viewing angles.

The **straightened** CPR (see Figure 11) projects the centerline of a single blood vessel or a path of a vessel tree (spanned across multiple blood vessels) fully elongated into the image plane. Each row in the image space corresponds to a specific sampling line in 3D at a given sampling distance along the vessel centerline. Showing the blood vessel completely elongated, distance metrics are pre-

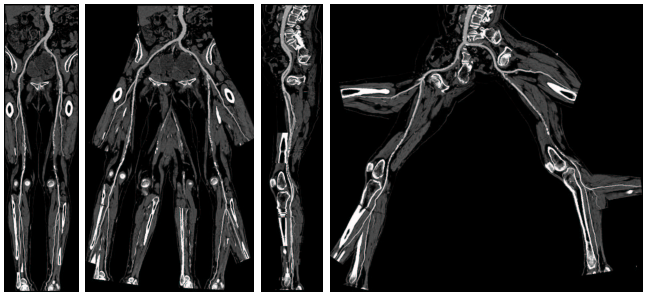

Figure 12: *Advanced CPRs of the vessels of a peripheral CTA dataset. (a) shows stretched mpCPR. (b) presents the untangled CPR of the same view. (c) displays a side view using again stretched mpCPR. (d) depicts the untangled CPR of the side view. (From [KWFG03])*

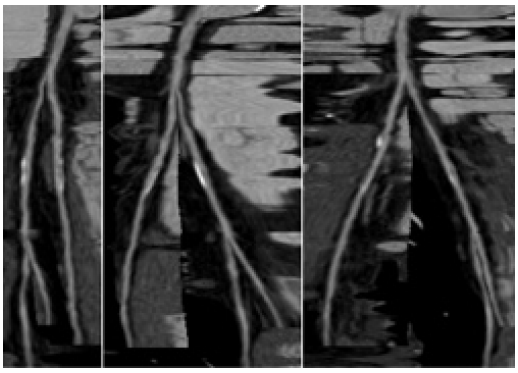

Figure 13: *Different views of the coronary arteries using TCPR. (Adapted from [LR06])*

served, hence isometry. But again, only the surface is generated by a vector of interest that is coplanar to the *xy*-plane. Distance can only be measured at the centerline. Straightening provides an unobstructed view of the vessel lumen, but the spatial relations are significantly deteriorated, as one cannot immediately recognize the spatial position of the vessel. Another limitation of the straightened CPR is the lack of overview over multiple vessels. Since the entire image space is consumed by the straightened resampled surface, each vessel requires a separate image. One possibility to alleviate this issue is to arrange several straightened CPRs in an anatomical manner [MMV*13]. Also the straightened CPR can be rotated by altering its angle of interest [KFW*02].

Resampling the CPR cut surface in 3D considers only a thin layer. Due to a possibly inaccurate centerline and small diameters of the blood vessels (e.g., lower limbs), taking a certain vicinity into account, enhances the overall stability of the visualization, as this improves the results in data sets with a low SNR. This can be achieved by computing a maximum intensity projection (MIP) or minimum intensity projection (MinIP) in a small neighborhood around the resampled CPR surface, resulting in a so-called **thick** CPR [KFW*02]. This can be done for all types of CPRs, the projected, stretched, and straightened ones.

In order to view the entire vessel lumen of a single vessel within one image, Kanitsar et al. [KWFG03] introduced the **spiral** CPR. This technique works as follows: firstly, straightening the centerline (*y*-axis) and, secondly, unrolling the spiral that starts at the centerline and progresses outwards (*x*-axis). Again, this method is image-based and depends on the chosen sampling strategy of the spiral, either a constant angle or a constant arc-length sampling. The advantage of the technique is a single image representing the entire interior of a blood vessel, compared to multiple CPR images, each representing a view at a specific angle. However, due to the spiral unrolling, this method is rather difficult to interpret. For example, an eccentric calcification is depicted by a repetitive pattern of high intensity values. One has to know this pattern in order to conclude that this represents an eccentric calcification. As the vessel is straightened, this method will preserve isometry if the vector of interest is coplanar to the *xy*-plane. Otherwise, if the spiral is perpendicular to the centerline, it will only preserve length measurements along the centerline itself.

The **untangled** CPR provides an obstruction-free view of the lumen of multiple CPRs [KWFG03], depicted in Figure 12(b) and (d). To achieve this, the authors introduce the *vessel hull* primitive that encloses the entire projected centerline of a single blood vessel. The vessel hull primitives of connected vessel centerlines should neither overlap nor touch in image space. If so, they are moved or rotated apart, but in such a way that they remain connected. Untangled CPR preserves isometry [KWFG03, KFWG06].

Zhu et al. [ZHT*02a, ZHT02b] propose a conformal mapping of tubular structures onto a planar polygonal area, based on the Laplace-Beltrami operator [AHTK99b]. They partition segmented blood vessels into Y-shaped regions and subsequently cut these surfaces open in order to map them onto a plane. Zhu et al. [ZHT03, ZHT05] extend their approach by introducing an area-preserving flattening of vascular structures. Their approach requires a surface mesh of the vessel tree and, again, they decompose the vessels into Y-shaped structures for flattening [ZHT*02a, ZHT02b]. The initial conformal flattening of these Y-shaped parts is determined using a finite element technique. By adjusting this conformal mapping using optimal mass transport theory, an area-preserving mapping is created [ZHT03].

Lee and Rasch [LR06] present a topological invariant transformation that resembles projected mpCPRs, referred to as *tangential curved planar reformation (TCPR)*. By sampling perpendicularly to the centerline, the interior of blood vessels is well shown, however, the surrounding tissue deteriorates. Multiple CPRs are created by means of image partitioning, as presented in Figure 13. As it resembles a projected CPR, it is neither isometric nor conformal.

Cai [Cai07] introduces a surface reformation technique that reveals the interior of blood vessels. By resampling a line, referred to as *director vector*, along the centerline curve, referred to as *directrix*, of a vessel, a ruled surface is created and subsequently projected either stretched or straightened into the image space. In order to provide an overview of the complete interior of a blood ves-

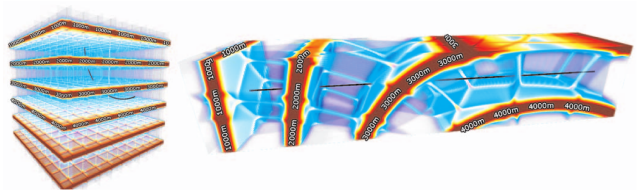

Figure 14: *A synthetic data set illustrating the curve-centric reformation. The left image shows a dataset with a curve inside. The right image shows the reformation, where the curve is straightened and volume deformed. (From [LCMH09])*

sel, they enclose the thin surface by the convex hull of the cross-sectional vessel shape. This hull is referred to as *biconvex slab* and rendered with, e.g., MIP. The outcome is a combination of a CPR with a MIP, without visual obstruction of structures with higher intensity values (e.g., bones), but with calcifications blending into the lumen. Stretching or straightening would preserve isometry and conformity, but the MIP of the biconvex slab does not.

Chiu et al. [CES*08] propose a flattening method for analyzing the development of plaque morphology between two examinations. Firstly, a 3D mesh of the common, internal and external carotid arteries is created from manually segmented ultrasound data. Then, similar to Zhu et al. [ZHT05], the mesh is cut longitudinally open to find an initial arc-length preserving map. To be able to assess the area-change ratio of the plaque, the initial map has to be transformed to an area-preserving map. In contrast to Zhu et al. [ZHT05], Chiu et al. define the density function outside the map such that it respects the mass-preserving condition and reduces the numeric errors of this transformation. Finally, the area-change ratio of the plaque is mapped to the flattened surface using a color map.

Lv et al. [LGZ08] present an approach that determines a contour that is easy to initialize for a gradient vector flow (GVF) snake model in order to segment the cross-section of a blood vessel. Their approach requires a user-specified contour that is approximated by a B-spline. Subsequently, points along this curve are traversed and along the ray between these points and the curve's center point the position with the maximum gradient is determined. This new set of points resembles the initial contour for the GVF snake. Once the cross-sections of the blood vessels have been segmented, a straightened CPR is used to inspect the lumen.

Lampe et al. [LCMH09] describe a curve-centric volume deformation along a 3D curve, see Figure 14. By conformally straightening the volume around the curve, comparative visual assessment of multiple data sets is offered. In order to provide an *inside-out* view of the reformatted data, radial ray-casting is employed and successively unfolded. Two application scenarios are presented, the first concerns the drilling exploration wells and well-bore uncertainty during real-time well drilling, whereas the second scenario investigates streamlines of a vehicle design simulation.

Angelelli and Hauser [AH11] propose a straightened view to assess and inspect the tubular flow in the human aorta and an exhaust system in a conformal manner. The straightening of the tubular flow

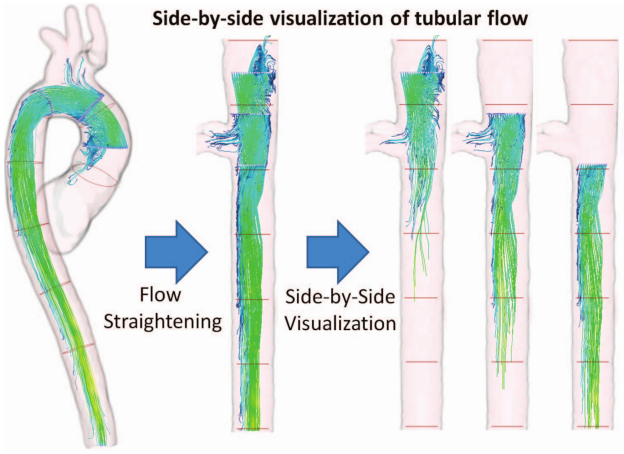

Figure 15: *Side-by-side comparison of straightened tubular blood flow in the human aorta. The three images on the right show the effects of different flow seeding structures. (From [AH11])*

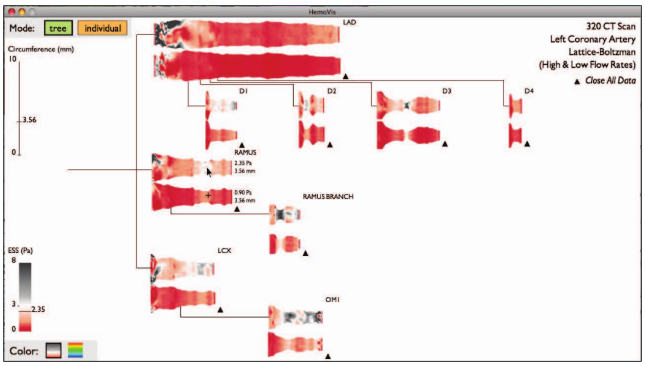

Figure 16: *The left coronary arteries arranged in a tree layout showing the ESS mapped to a red-black diverging color scheme. (From [BGP*11])*

is performed by transforming from the physical to the tubular and finally the straightened space. By arranging these views side by side, the flow of multiple timesteps can be analyzed as presented in Figure 15.

Borkin et al. [BGP*11] introduce a static anatomical layout for the investigation of coronary arteries shown in Figure 16. These arteries are first flattened using a pseudo-cylindrical projection, where the circumference is symmetrically drawn around the x-axis, and then arranged from left to right in image space. Child arteries are depicted below their parent vessels and connected with lines. The endothelial shear stress (ESS) is visually encoded on this flattened surface using a diverging color map. Several layout strategies and color maps, among them the rainbow color map, have been evaluated.

Mistelbauer et al. [MVB*12] introduce **centerline reformation (CR)**, an extension to a projected mpCPR, that allows cutting through spatially arbitrarily oriented blood vessels, as shown with the cross-over bypass in Figure 17(b). Analogously to a projected

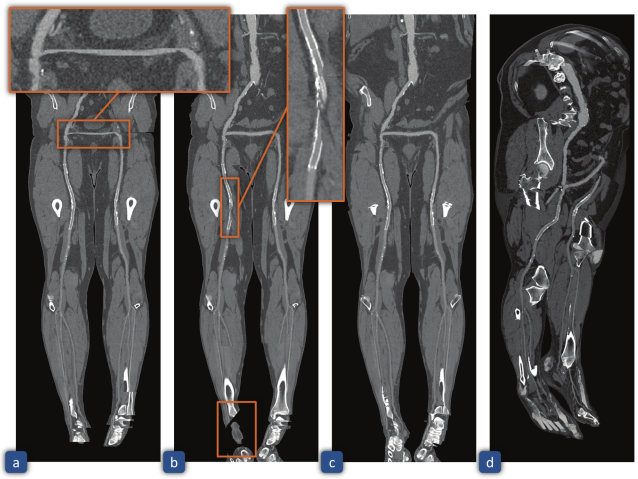

Figure 17: *Comparison of vessel reformation techniques along the vessels of the human lower extremities. (a) shows a mpCPR depicting the cross-over bypass too narrow. (b) presents CR that correctly renders the bypass, but a large cut through the surrounding tissue leads to visibility issues. (c) demonstrates CSR that displays the lumina of all blood vessels without problems. (d) renders the lumina from a different viewing angle using CSR with a context visualization around them. (From [AMB*13])*

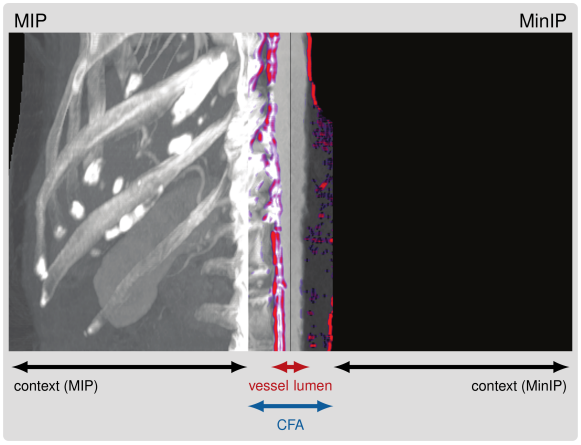

Figure 18: *Example of a CFA of a single vessel segment. The vessel lumen is shown in the center of the image and the overlay (from red being unstable to blue being stable) depicts the stability of the centerline. Outside and around the CFA a context visualization is rendered, MIP in the case. (From [Mis13])*

mpCPR, the centerlines of the blood vessels are first projected into the image space. Subsequently, a wavefront propagation algorithm renders the lumina by growing from the centerline outwards. The arc-length distance along the centerline is used to provide a correct visibility of overlapping blood vessels by determining whether a pixel is closer to the viewer or not. Due to the projection, CR does neither preserve isometry nor conformity.

Auzinger and Mistelbauer et al. [AMB*13] further extend mpCPR and CR by employing a 3D ray-casting approach to render the interior of multiple blood vessels, referred to as curved surface reformation (CSR) and demonstrated in Figure 17(c)-(d). As projected CPR and CR, CSR does neither preserve isometry nor conformity. The core aspect of the method is the use of a cost function that weights the distance to the viewer with the normal distance to each centerline—both computed for each sample along each ray. To provide interactive frame rates even for larger CTA datasets ($512 \times 512 \times 2000$ slices) the method has been implemented in CUDA. Since minimal centerline variations could lead to large surface variations at larger distances to the centerline, a level-of-detail (LoD) approach is employed by successively smoothing the centerline with increasing distance. This retains details close to the centerline while simultaneously offering a smooth cut through the surrounding tissue. At the same time, CSR implicitly respects the visibility of several overlapping blood vessel, through the cost function.

Diepenbrock et al. [DHS*13] propose **normalized circular projection (NCP)**, a method that analyzes the development of a carotid stenosis in mice using positron emission tomography (PET)/computed tomography (CT) data. In order to expound the multimodal data in a single image, NCP straightens the blood vessels and subsequently expands them to a cylinder, with its radius defined as the inner vessel radius, excluding the vessel wall thickness. They use circular rays within cross-sections perpendicular to the centerline and employ a MIP to obtain one value. This creates a single image to assess the PET activity along the corresponding blood vessel. Since intensity values are radially aggregated, neither an isometry nor conformal mapping is obtained.

Mistelbauer et al. [MMV*13] introduce **curvicircular feature aggregation (CFA)** that summarizes several CPRs in one image by aggregating them—an operation that is neither isometric nor conformal. Normally, CPRs are rotated around an axis, whereby a point in a plane normally follows a circle along the rotation axis. This principle is used to aggregate all CPRs virtually circularly in perpendicular cross-sections along the centerlines. Several techniques can be used for this purpose that highlight specific data aspects. The points along these circles or circular rays can be used to combine several techniques to highlight specific data aspects. For example when using CTA data, MIP highlights calcifications, but MinIP emphasizes soft plaque. These two aspects are important for the analysis of vascular stenosis. Figure 18 provides an example of a CFA with MIP on the left side and MinIP on the right. The stability overlay indicates the robustness of the centerline under local perturbations. A context is rendered outside the vessel lumen around the CFA.

Cui et al. [CWW*16] describe an approach for cross-sectional lumen area quantification in order to assess stenoses of coronary arteries. They segment the vessels using multiscale vessel enhancement based on Frangi's vesselness and centerline extraction. Subsequently, these vessels are straightened based on the approaches of Lampe et al. [LCMH09] and Angelelli and Hauser [AH11]. These straightened views offer the possibility to visually compare different methods employed for cross-sectional luminal area quantifica-

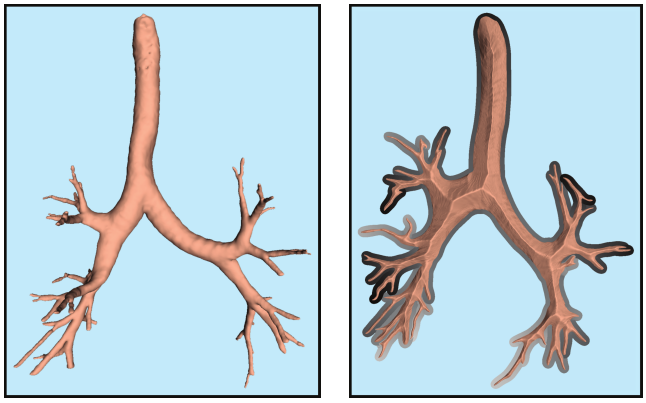

Figure 19: *Planar embedding of a bronchial tree. (a) displays the tree in projection direction. (b) shows the resulting planar visualization with depth cues encoded into the border with darker indicating closer to the viewer. (From [MK16])*

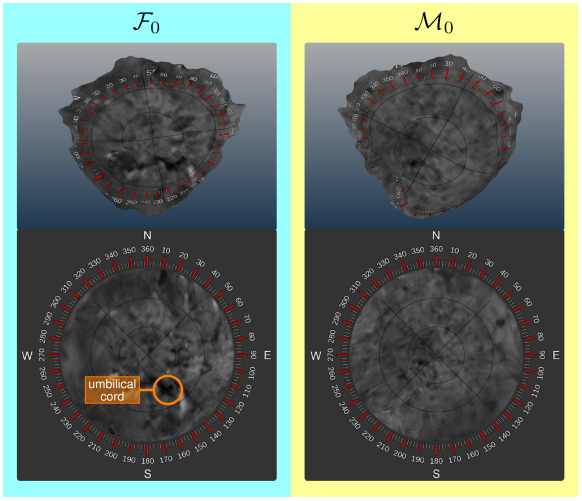

Figure 20: *Example of placenta maps showing the fetal side on the left and the maternal side on the right. The top row depicts the 3D structure of the corresponding placenta sides, whereas the bottom row presents the flattened visualizations respectively. On the fetal side one can see the umbilical cord. (Adapted from [MMK*17])*

tion. However, this mapping does not retain isometry but conformity.

Marino and Kaufman [MK16] describe an approach for creating planar embeddings of tree-like tubular structures while simultaneously retaining the spatial relation or shape. Firstly, the skeleton of the tree structure is projected to the image plane using a radial planar embedding. Since this does not preserve the shape of the object, it has to be reconstructed using the estimated radii and the projected angle between two consecutive edges. This iterative algorithm successively rotates a sub-tree while accounting for no intersection. Once every edge is rotated to a certain extent, the algorithm terminates and the 3D shape has been restored. Secondly, by employing a quasi-conformal mapping that is solely based on harmonic mapping, the surface of the object is flattening into the plane. In order to enhance the depth perception of the flattened tree, color-coded contours are added around the segments from white to black representing the depth, see Figure 19.

3.2.4. Placenta Maps

Miao et al. [MMK*17] introduce an approach to assess the health of the human placenta in-utero. The data of the placenta is acquired using magnetic resonance imaging (MRI) and subsequently post-processed to compensate the fetal movement. The placenta is then extracted and split into the maternal and fetal sides, as depicted in Figure 20. Both halves are flattened into circles as this procedure resembles the ex vivo shape of the analyzed placenta. Their technique is based on the *mean value coordinates* by Floater [Flo03] and approximate discrete conformal maps. To inspect structures that exhibit a certain depth into the placenta, such as the cotyledons, a distance field is computed to offset the surface of the placenta inwards and outwards as well.

3.3. Usage Guidelines

As discussed above, generating 2D surfaces from complex 3D surfaces is a widely used approach in the context of the circulation system. Which kind of parameterization should be used for the flattening depends on which tasks the resulting 2D structure should be used for. In the context CVDs, measuring specific spatial distances, such as the diameter, could be a required task. For this purpose, an area-preserving flattening should be applied if conformal parameterizations would lead to distortions resulting in erroneous measurements. For generating overview visualizations of the vasculature, conformal, or area-preserving techniques could be used, such as by Meuschke et al. [MVB*17], where at least for aneurysm data occurring distortions are not disturbing. Moreover, also more abstract depictions can be used, which are neither angle-nor area-preserving. However, the clinicians should be familiar with this kind of visualization to avoid long training periods. For a more detailed data exploration, a visual combination of the 3D and 2D surface visualization is suggested, which provides a spatial correlation between both depictions. The 2D representation could be used for highlighting interesting regions that can then be observed in more detail using the 3D representation. For comparing datasets, a parameterization is appropriate, which maps the vasculature to a uniform structure such as a sphere [GSK*12].

4. Application: Colon Unfolding

Colorectal cancer is one of the leading malignancies in the Unites States [SMF*17]. It is often diagnosed using colonoscopy and medical imaging techniques like MRI and CT.

4.1. Tasks and Requirements

To obtain a scan of the abdomen, patients are usually scanned in both supine (facing up) and prone (facing down) positions. These scans are then registered for further processing. The colon, also called *lage intestine*, consists of the following five main sections: cecum, ascending colon, transverse colon, descending colon, and sigmoid colon.

Abnormalities, such as polyps in the colonic wall, are a major requirement to be preserved during flattening. The general problem with their detection is the occlusion through haustral folds and the natural bending of the colon. This task can be significantly alleviated if the whole surface is visible in a single view and/or supported with volume or 3D endoluminal renderings to assist the physician in navigation and diagnosis [MK10]. The polyps should remain clearly identifiable and visible in the flattened representation and maintain their features for an efficient detection.

To gain insight into the internal structure of polyps when flattened out, electronic biopsy can be utilized [MDB*11]. When CT data is rendered using a translucent transfer function mapping higher densities to red and lower densities to blue, benign tissue and adenomas can be differentiated. The former will appear as homogeneously blue and the latter as irregular red.

4.2. Techniques

Haker et al. [HATK00a, HATK00b] provide an analytical approach for virtual colon unfolding based on a triangle mesh representing of the colon surface. This surface is then flattened onto a plane in a conformal manner by employing a finite element-based technique. To account for the induced area distortion due to mapping the surface to a rectangle, the authors propose an optimized—in a least squares sense—view of the flattened colon.

Bartroli et al. [BWKG01] introduce nonlinear unfolding of the colon surface. Their method overcomes double appearances of polyps as well as geometrical deformations and undersampled surface parts. Based on the centerline of the colon, a nonlinear ray casting is performed, which yields a 2D cylindrical parameterization of the inner colon surface. Moreover, for each vertex the distance to the nearest centerline point is calculated, yielding a distance map. For each point of the centerline, rays are traced towards the colon surface, following the negative gradient of the distance map. This results in a sampling of the inner surface, in which the distances between the rays start points and intersected surface points determine a height field. Then, the height field is unfolded. To avoid geometric deformations, an iterative scaling is applied to the height field, to preserve areas of the surface patches and edge lengths. Finally, the 2D grid representation of the colon surface is resampled to correct missing surface features.

Lee et al. [LLS05] propose a fast algorithm for generating an unfolded view of the colon to assess polyps. For this purpose, they compute ray templates at control points perpendicular to the centerline of the colon. Since these rays might intersect at regions with high curvature, the ray templates at the control points are first checked whether they are intersecting. If this is the case, the rays are successively moved to form a conical template. To fill the region inbetween control points, the ray templates are linearly interpolated. This offers a denser sampling while avoiding any intersections that potentially lead to missing or duplicating pathological findings.

Hong et al. [HGQ*06] present a general technique to conformally map the colon to a planar rectangle which is able to deal with surfaces of arbitrary genus. First, they apply topological denoising to remove handles at their shortest loop. This processing is applied to reduce noise, and therefore distortions during flattening. Second, the parameterization is then performed by solving an elliptic partial differential equation to minimize the harmonic energy of the map using the finite element method. Afterwards, direct volume ray-casting is utilized to presents the colonic surface in a natural fashion to the physicians, contrary to, e.g., Haker et al. [HATK00b] with their mean curvature color-coding. To ray-cast the colon, they place several uniformly spaced cameras along the centerline and separate the geometry into segments.

Mai et al. [MHS07] perform a cylindrical parameterization of the colon as an intermediate step before cutting it open and unfolding it onto the plane. Different in their approach is the way how they cut open the topological cylinder of the colon. They traverse along the gradient of the harmonic mapping function which continuously increases from one cylinder's base to the other. During this process, triangles can also be split. The result is a flattened colonic surface with preserved circumferential geometry. The presented approach does not maintain any particular distortion property, neither angles nor areas. To visualize the generated 2D map, Mai et al. color the colon using the distance information, obtained by computing a *chamfer distance transformation*, from the colonic centerline to the geometry's surface. Normal mapping is then applied to enhance shape perception, especially of polyps.

Williams et al. [WGC*08b] introduce a combination of CPR (context) and volume rendering (focus) for virtual colonoscopy. First, a CPR along the centerline of the colon is rendered and the interior of the colon marked for volume rendering using an approach based on region growing to ensure including all relevant parts. Second, depending on the type of CPR (projected, stretched, straightened), volume rendering is done for the marked region by casting rays from the centerline until they hit the inner wall of the colon.

To register and visualize CT scans in supine and prone position for virtual colonoscopy, Zeng et al. [ZMG*10, ZMGK10] present a quasi-conformal mapping approach. First, the colon is separated into its five anatomical segments by the extraction of the *taeniae coli* and flexure landmarks. The obtained sections are then conformally mapped to the plane. Graph cut-based energy minimization is applied to detect and match features between the supine and prone surfaces, coded with their mean-curvature. A harmonic map is then used to align all associated segments in a quasi-conformal way due to the deformations between the supine and prone scans. The final registration is a diffeomorphism, a smooth, one-to-one mapping which is invertible. Zeng et al. adapt the ray-casting visualization method from Hong et al. [HGQ*06] and place the supine and prone colon images side by side. This enables the physician to simultaneously detect and verify polyps in both scans.

To improve the spatial orientation for guiding navigations, Marino et al. [MZGK11] present a context-preserving approach

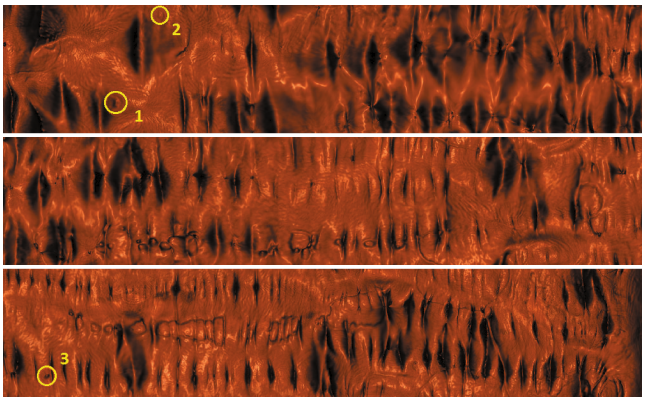

Figure 21: *Flattening of the entire colon, starting with the rectum on the left side of the top image and ending with the cecum on the right side of the bottom image. The haustral folds and colonic polyps (yellow circles) are well preserved. (Adapted from [GSZ*13])*

to flatten tubular structures. In the colon's case, its centerline is orthogonally projected onto the 2D plane and adjusted such that the overall length is maintained and no overlap is present between segments to ensure an occlusion-free view. Neighboring areas are spatially arranged in a way that there is enough space for the colon's boundary when sliced open and placed along the skeleton. A conformal map is then generated using the discrete Ricci flow and harmonic mapping to arrange the 3D surface inside the given 2D boundary while preserving the overall geometric context and features.

Zeng et al. [ZMKG11] describe an automatic volumetric flattening method which uses the whole colonic wall instead of a surface representation. This has the advantage that more complete and precise information is available which can be used to generate accurate rays for volume visualizations. The obtained tetrahedral mesh is then rendered using the cell projection method [ST90]. Other methods have to use the colon's surface together with the centerline or surface normal which can lead to slightly incorrect results. Overall, their approach is computationally efficient as only sparse linear systems have to be solved.

The approach from Gurijala et al. [GSZ*13] focuses on robustness for colon flattening and registration tasks. By using a heat diffusion metric instead of the Euclidean metric, their algorithm becomes insensitive to noise in the topology, such as handles which frequently occur due to reconstruction errors. This enables a more robust flattening because no prior denoising, neither manually nor automatically, has to be applied first. The presented method is general because it processes topologies with inner holes and handles and can map to an annulus or rectangle. They also introduce a technique to remove the still present artifacts in the flattened representation. A completely flattened colon representation is presented in Figure 21 with three polyps depicted by yellow circles.

Lu et al. [LZ14] present a virtual flattening of the inner colon surface focusing on the correction of deformation distortions. For this purpose, usually the inner colon surface is used. In contrast,

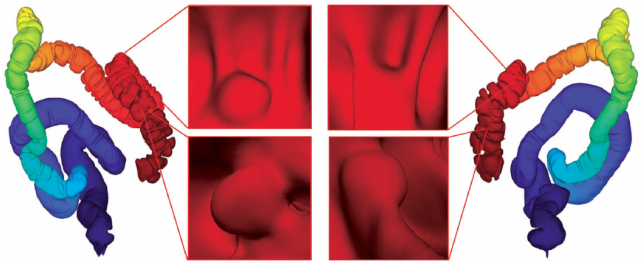

Figure 22: *Supine (left) and prone (right) view of the colon in Fiedler vector representation with corresponding color coding. It is obvious that there is a difference in the CT scans between these two positions of the patient. The appearance of polyps differs or they can even be completely missed in one of both data sets. (Adapted from [NMGK17])*

they use the outer surface of the colon because it possesses fewer colonic haustral folds. For the extraction of the colonic outer surface the level set method is applied. Moreover, they use a geodesic distance map to eliminate merge artifacts in the generated mesh between distant colonic regions. These artifacts originate from the level set method if two surfaces are close to each other and get not correctly separated. Finally, distortions of the flattening are corrected using a ray-casting approach. To generate a homogeneous sampling, curved and straight regions are independently processed.

Nadeem et al. [NMGK17] present an approach to register and visualize supine and prone colon surfaces based on haustral fold matching. A Fiedler vector representation of the geometry serves as basis for their method. The Fiedler vector is the second eigenvector of a mesh's Laplacian and allows to find, among other applications, a natural ordering of its vertices. Nadeem et al. use this property to initially register two instances of a colon's supine and prone model on the global scale. Level sets are then computed on the Fiedler vector to segment haustral folds by curvature analysis. These are then used to improve the initial registration though fold matching between the supine and prone data set. Finally, the colon is cut open and flattened using a slightly modified version of the method from Zeng et al. [ZMG*10]. Figure 22 shows the same colon data set in supine and prone view with a different appearance of polyps.

4.3. Usage Guidelines

Concerning the preservation of polyps in the flattened representation of the colonic surface, their shape has to be well preserved either for manual or automatic detection. To achieve this, conformal parameterization methods are better suited. However, as the area is not considered in these mapping algorithms, polyps can shrink such that they are no longer sufficiently represented in the final representation. Equiareal techniques, or at least area-preserving characteristics, have to be incorporated into these algorithms to counteract this problem.

To register two instances of the colonic surface, conformal parameterizations are again to be favored. They preserve features necessary to formulate correspondence constraints for the alignment.

5. Application: Brain Flattening

The highly convoluted surface of the brain with its Gyri (ridges) and Sulci (depressions or fissures) demands flattening algorithms to allow a visualization of deep buried features in an occlusion-free manner without the need for interactive exploration. To realize the flattening, in most cases meshes are extracted from the volumetric data set which are then flattened to the sphere, circle, or plane. Magnetic Resonance Imaging (MRI) and the dynamic functional Magnetic Resonance Imaging (fMRI) are two modalities frequently mapped with these techniques, in order to examine the brain's anatomy, pathology, and activity in a non-invasive way.

5.1. Tasks and Requirements

Registration is usually the first step for intra- and inter-subject comparisons or the superimposition of functional data (e.g. fMRI measurements) for topographic maps (e.g. in retinotopy or tonotopy). This is essential, as the variability analysis of sulcal patterns across subjects can even be performed to compare different species. Only if multiple data sets are in a common coordinate system, statistical comparison and combination of anatomical brain models will be possible. To achieve parameterization results which can then be used to register different brain data sets, landmarks or atlases are often used. Landmarks alone are not sufficient for registration tasks, geometric features in between can still be distorted. One solution is to align landmarks and features inside the parameterization domain itself which can be transferred back to the original space. However, not every flattening method is tailored for this task and supports a spatial alignment of different data sets.

The detection of brain abnormalities and the progression over time in morphology and morphometry studies is applied in the research field of disease patterns like Alzheimer's, Parkinson's, Williams syndrome, or Schizophrenia. Properties such as the neuronal density, cortical functional activation extent, or cortical thickness variations, are used to examine pathological conditions. Cerebral Atrophy (shrinkage of the brain) is for instance an indication for Alzheimer's Disease or Parkinson's Disease. Therefore, Gray Matter and White Matter segmentation is often applied on the flattened cortical sheet for further inspection. Furthermore, functional and structural symmetry studies are performed between the left and right hemisphere to analyze and visualize the influence of disease, age, gender, handedness, or the development of the brain. In the following section we will describe techniques, which have been proposed for brain flattening.

5.2. Techniques

Angenent et al. [AHTK99a, AHTK99b] generate conformal maps of the brain's surface by solving a second-order elliptic partial differential equation using the finite element method. They use a fixed north pole mapping to the complex plane by solving a set of linear equations. As they deal with genus zero closed brain surfaces, inverse stereographic projection can be used to transform the planar map to the spherical domain.

Goebel [Goe00] presents a cortical surface flattening algorithm which starts with smoothing the initial 3D data set to remove non-biological surface irregularities as Van Essen et al. [VED97] have proposed earlier. The goal is to parameterize each hemisphere of the brain on a planar domain. Therefore, the geometry is first inflated and cut into multiple pieces. After projecting every part towards the plane, an iterative scheme minimizes metric distortions.

Timsari and Leahy [Tim99, TL00] propose a quasi-isometric mapping scheme which does not directly perform a length-preserving flattening, but rather combines conformal and equiareal constraints to flatten towards the planar domain. A cost-function which expresses flatness through convexity is combined with an angular and area constraint. The optimization is performed using the conjugate gradient method. Therefore, an additional functional to smooth the cortical surface is necessary to rather end in a global than a local optimum. To flatten the whole cortical surface, their approach first inflates the topological sphere of the brain. By introducing a cut, two hemispheres can be obtained and flattened towards the plane.

Wandell et al. [WCB00] focus on the flattening of smaller regions of the brain to study functional activity. They also identify problems when using imaging modalities in combination with different spatial resolutions such as MRI and fMRI. They state that activities detected in the spatial neighborhood of the fMRI scan do not necessarily reflect the same neighborhood on the surface of the cortical sheet extracted from MRI. Initially, the described parameterization places equidistant sampling points in concentric circles on the cortical surface, from which a planar graph is generated and laid out on the 2D plane. In the next step, the distances between these samples are iteratively optimized.

With a sphere as target topology, Gu et al. [GWC*04] compute a homeomorphism between two genus zero manifolds, specifically the cortical surface. First, an initial mapping is calculated using the steepest descent method which minimizes the harmonic energy to ensure conformity. Here, the resolution of the input meshes is not relevant. To obtain a unique solution, zero mass-center and landmark-based constraints are used to form optimal Möbius transformations. Gu et al. demonstrate their method with the conformal mapping of cortical surfaces to a sphere. With the obtained unique parameterization, spherical harmonics can be used to smooth and compress the given geometry as shown in Figure 23. Using the harmonic coefficients, two brain surfaces can even be compared without the need for registration.

Hurdal et al. [HBS*99, HS04, HS09] discuss the application of circle packing to generate conformal parameterizations. The target domains, to which circle packing algorithms can flatten surfaces onto, are a sphere, disk, or plane. Additionally, the advantages over the usage of numerical partial differential equations for conformal mapping are illustrated. Their main targets are smaller regions of interest to avoid more severe distortion which occurs when conformally mapping geometry with a small open boundary compared to its overall size. However, a whole hemisphere can be flattened as well.

Joshi et al. [JSTL04] apply *p-harmonic energy* minimization to cerebral cortex data sets to generate comparable parameterizations. The smoothness of the resulting maps is dependent on the order of the p-th norm. However, a conformal map can only be produced using $p = 2$. Each hemisphere of the brain is first mapped to the unit disk. Afterwards, the p-harmonic map is obtained through a

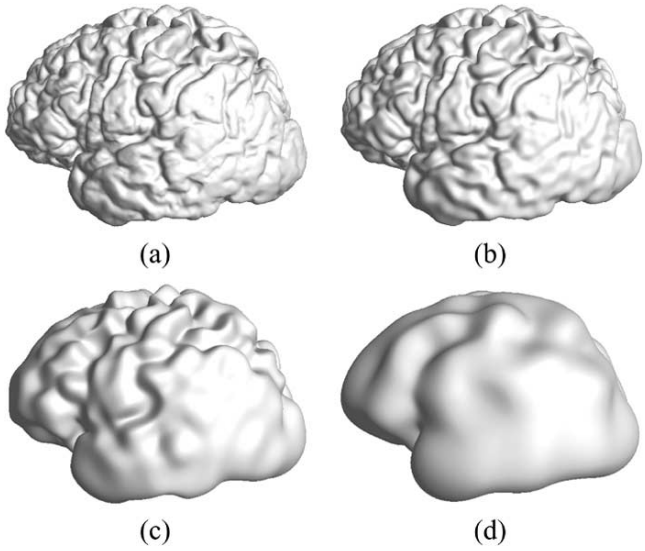

Figure 23: *If the target domain for the parameterization is a sphere, spherical harmonics can be utilized to low-pass filter geometry through the removal of coefficients. The initial brain geometry is shown in (a). Surfaces (b), (c), and (d) are smoothed out representations, reconstructed from a decreasing number of coefficients. (From [GWC*04])*

finite elements approach. Stereographic projection is finally used to conformally map both unit disks onto a unit sphere.

Ju et al. [JSR*04] use least squares conformal mapping (LSCM) presented by Levy et al. [LPRM02] to generate parameterizations from cortical surfaces to planar and spherical domains depending on the input's topology. Beside the minimization of conformal distortion, metric constraints are added using the geodesic distance. Finally, they compare their approach to the software packages *FreeSurfer* by Fischl et al. [FSD99] and *CARET* by Drury et al. [DVEA*96] and achieve a significant speedup whilst scoring similar distortion values. An additional comparison paper by Ju et al. [JHS*05] extensively evaluates three different methods (FreeSurfer [FSD99], CirclePack [HSS*99], and LSCM [JSR*04]) in terms of distortion and computation speed.

Pons et al. [PKF04] present a mathematically exact, area-preserving mapping algorithm which is based on a normal and tangential motion used in an iterative deformation process. The goal is to transform the highly convoluted cortical surface into an inflated representation. As the type of input, triangle meshes or level sets of arbitrary dimension and topology can be devoted. They compare their approach to Fischl et al. [FSD99] which produce similar results, although they do not consider area distortion directly. The advantage of this algorithm is that it also applies to an arbitrary topology, not only genus zero surfaces.

Stylianou and Farin [SF04] use the extraction of crest lines on the cortical surface for segmentation and flattening. At first, crest lines are identified and used to segment regions using a geodesic Voronoi diagram. Tutte's *barycentric surface flattening* [Tut60, Tut63], as well as *weighted mapping* and *mean value coordinates* by Floater [Flo97, Flo03] are extended to speed them up by the usage of this diagram. Finally, they compare all three extended approaches in terms of area preservation. Their conclusion is that mean value coordinates preserve the area component of the parameterization best.

Tosun et al. [TP01, TRH*04, TRP04] present a mapping technique to flatten the cortical surface to a sphere to study thickness changes in aging. To be able to compare multiple brains, an atlas brain is selected which serves as a reference, and a common north pole is chosen to align all subjects. Furthermore, both hemispheres of the brain area are treated separately to avoid distortion problems. First, an intermediate, inflated version of the cortices is calculated using the relaxation scheme from Drury et al. [DVEA*96]. Then, all brains of interest for later analysis are registered to the atlas using a modified iterative closest points algorithm to enable cortical comparison. An optimized, conformal map from the atlas brain to the sphere is calculated using the algorithm from Angenent et al. [AHTK99b] combined with an inverse spherical projection. Since all brains are registered, the parameterization from the atlas can finally be used to map all inflated parts conformally and anatomically consistent to the sphere for further processing and visualization. Overall, the presented procedure yields quasi-conformal maps with optimized area distortion.

Wang et al. [WGC*04a] propose a conformal brain mapping technique to the sphere which also allows to map two genus zero surfaces in general. While minimizing a harmonic energy functional to find a homeomorphism, constraints are added to obtain a converging and unique solution. Using Möbius transformations determined from cortical landmarks, two conformal maps can be optimized to enable the comparison between data sets. The presented approach is thus independent of the mesh triangulation.

Wang et al. [WGC*04b] calculate a volumetric harmonic mapping from the brain to a solid sphere. Beside the extractable, 2D cortical surface, imaging techniques also provide information about interior structures. By creating a volumetric parameterization, brain morphometry can be studied on the whole information available. The cortical surface is first conformally mapped to the sphere by means of previous techniques [GWC*04, WGC*04a] serving as a boundary condition. The harmonic energy of the map is then iteratively minimized by means of a heat flow method.

The algorithm presented by Memoli et al. [MST06] minimizes the global Lipschitz constant of a map which serves as measure for the geodesic deformation of the surface parameterization. This distortion metric is based on geodesic distances while respecting provided boundary conditions such as fixed curves or points in the map. Their iterative algorithm is also suitable for the direct registration of cortical surfaces without any intermediate flattening step. While brain surface registration is their main motivation, a sphere or other flat geometries as targets are also possible.

Kwon et al. [KHP08] propose a two-step algorithm to flatten the cerebral cortex onto a sphere. They do not strive for any particular type of preservation. The overall linear distortion is minimized during the process. For all computations, the vertices are represented in polar coordinates. As a first step, all vertices of the brain are projected onto the sphere using the *accretion of concentric rings*

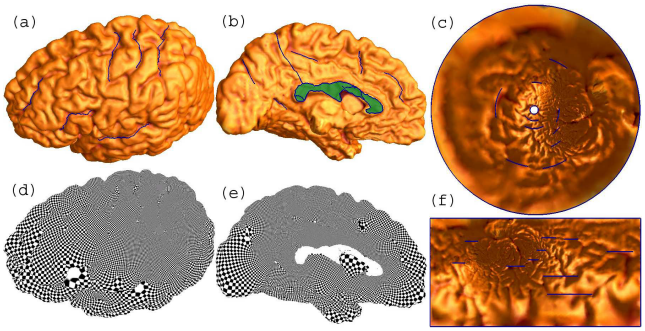

Figure 24: *Conformal mapping of a cortical hemisphere, with landmark cuts in blue (a, b) and an open boundary in green (b), to two different target domains. A circular (c) and a parallel slit map (f), where contrary to [WSY*12] the landmarks in the final map are closed and not open features, see Figure 27. The result, when overlaying the parameterization back onto the original brain surface is shown in (d) and (e). (From [WGC*08a])*

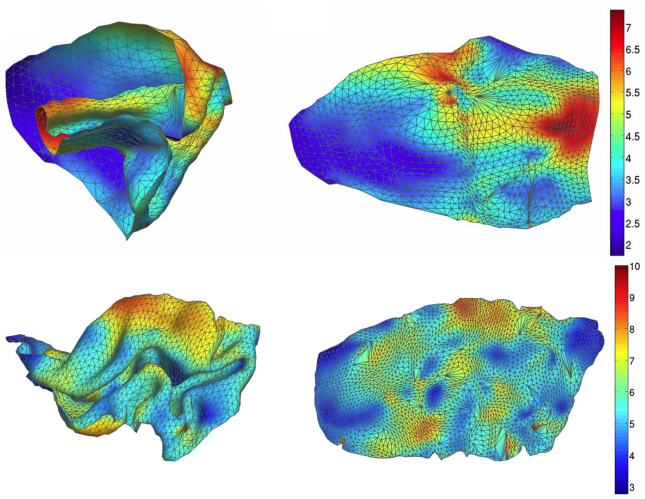

Figure 25: *Quasi-isometric flattening of the visual area V1 from a macaque (top) and a human (bottom) generated to study the similarity of their intrinsic shape [HPR*08]. On the left, the original geometries are shown with their flattened version on the right side, respectively. Color-coded per-vertex error values from low (blue) to high (red) reveal areas with larger distortion. (Adapted from [BPS10])*

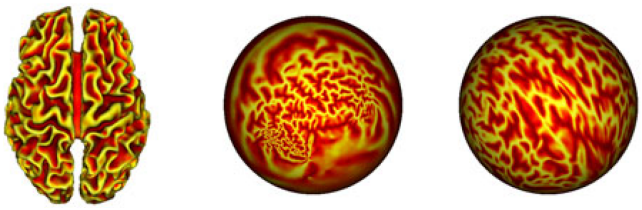

Figure 26: *The original cortical surface (left) is first conformally mapped to the unit sphere (middle) using previous techniques [GWC*04]. In the second step,* Lie advection *it is applied to evolve the initial, conformal map to an area-preserving parameterization (right). (From [ZHGH11])*

method by Drury et al. [DVEA*96]. An iterative smoothing is applied to untangle overlapping polygons. Finally, the linear distortion of the parameterization is iteratively minimized.

The conformal mapping of the cortical surface with multiple, open boundaries is presented by Wang et al. [WGC*08a]. As target domain, a punctured annulus or a rectangle can be chosen. Landmark curves of the cerebral cortex are cut open and flattened to the parameter domain such that they appear concentric or parallel, as shown in Figure 24. These so called slit maps are calculated in a linear fashion and yield globally conformal results. Different landmark features can be chosen to serve as inner and outer boundary condition. An advantage over Wang et al.'s approach [WLG*07] is that slit maps do not produce singularities.

Balasubramanian et al. [BPS10] introduce a near-isometric flattening algorithm based on the earlier work of Schwartz et al. [SSW89]. Their target domain is arbitrary as long as it is a manifold (locally Euclidean). The given geometry is simply flattened out such that the isometric distortion is minimized (see Figure 25). Two main steps are performed in their process. At first, the calculation of the *exact* geodesic distances between all pairs of vertices of the input mesh is performed. Second, based on an initial flat map with an area equal to the original one, the error of the parameterization is iteratively minimized with the constraint to not produce edge crossings. They also propose a set of six criteria which near-isometric flattenings must fulfill together with a set of test surfaces for their evaluation. The presented algorithm meets all these criteria, but is only applicable to meshes with an open boundary (which can easily be obtained by deleting a single vertex) and no handles. Their evaluation exhibits a high similarity of the visual cortex between subjects, likewise for brains from humans and macaques.

Lui et al. [LTW*10] employ landmark curves on cortical surfaces to generate conformal maps for registration tasks. In the beginning, an initial conformal parameterization is obtained by using Wang et al.'s algorithm [WLG*07] described earlier. Through the minimization of an energy functional represented by a vector field, a shape-based diffeomorphic mapping function is obtained, which simultaneously preserves the conformal property and aligns all landmark curves inside the parameter domain.

Lie advection is used by Zou et al. [ZHGH11] to develop an area-preserving mapping when an already flattened diffeomorphism is given as input, or can be calculated in a first pass (see Figure 26). As final target domains, the unit square and sphere are presented. By use of the Laplace-Beltrami operator, a gradient vector field is computed and integrated over time to create a diffeomorphic flow. This iterative scheme transforms any initial map into an area-preserving parameterization.

Wang et al. [WSY*12] use the Ricci flow method to conformally flatten cortical surfaces and formulate it as a circle packing problem. They introduce intentional cuts along landmark curves which can be mapped to specific locations in the parameter do-

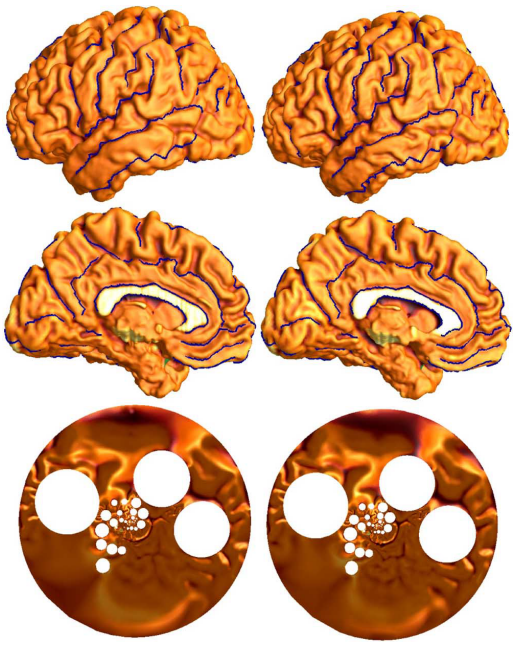

Figure 27: *Two conformal mappings to the unit circle of the same cortical hemisphere surface (top and middle), scanned at two different points in time (left and right respectively). Landmark cuts (blue) make it possible to register these specific areas in 2D and to reduce the overall distortion which can be seen in the similarity of the two generated parameterizations (bottom). (Adapted from [WSY*12])*

main (see Figure 27). This allows an easy registration between different data sets and the handling of difficult topologies with boundaries. The target curvature space may also vary. A mapping to the disk, rectangle, or square, all with optional holes, is demonstrated. The Ricci flow minimization is computed using Newton's method with an existing global optimum. A study on brain asymmetry between the left and right hemisphere is performed to examine and visualize the influence of diseases, age, or the development over time.

Based on Monge-Brenier theory, more specifically on optimal mass transport, Su et al. [SZS*13] present an area-preserving brain mapping to flatten cortical and caudate nucleus surfaces. First, a conformal map is calculated using the discrete Ricci flow method introduced by Wang et al. [WSY*12]. Followed by the computation of a *power Voronoi diagram* and a *dual power Delaunay triangulation*, a unique and diffeomorphic map onto the unit disk is obtained. The brain parameterization is also intrinsic to the Riemannian metric and invariant to isometric transformations.

Auzias et al. [ALLT*13] build on the parameterization model from Clouchoux et al. [CRM*10] to create rectangular maps for surface matching tasks. Sulcal landmarks are axis-aligned and conformally mapped onto an orthogonal referential system. This strategy has advantages over the direct mapping between two brain surfaces, e.g. if a Sulcus consists of multiple segments instead of a single one. These segments can still be mapped onto the same axis in the model. They further adapt their model-driven approach to enable the mapping to fetal cortical surfaces with different gestational age to this planar domain [ADGP*15].

Usually, brain surface flattening methods consider only one single extracted surface. Khosravi and Soltanian-Zadeh [KSZ14] present a quasi-isometric parameterization scheme which takes multiple layers of the cortex into account. This work is motivated by the fact that features can be present within the tissue between the pial surface and the white matter. Multiple layers with local axis per vertex are set up pointing orthogonally towards the outer surface. All layers are flattened simultaneously via optimization which only uses rotational operations to maintain the isometric properties as much as possible.

In order to perform cortical surface registration, Choi et al. [CLL15] propose a method which quasi-conformally maps to a sphere and a triangle as intermediate steps. As an initial step, the brain's surface is conformally mapped onto a sphere using the method from Angenent et al. [AHTK99a]. Emerging distortions on the north and south pole of the spherical map are then minimized through an algorithm which uses the inverse stereographic projection onto a big triangle to linearize further problem solving. Conformity distortions are then fixed on this flat representation. The outcome is a quasi-conformal landmark-aligned spherical harmonic map between two brain surfaces with guaranteed bijectivity that is free of flips and overlaps. An additional iterative step also establishes the diffeomorphic property or their parameterization.

5.3. Usage Guidelines

In general for brain flattening, one has to separate between the preservation of topological and geometrical structures. Using the topology itself is more suitable for pattern analysis and visualization-related tasks. Geometric structures need to be preserved if the measurement of quantities in the flattened domain is the primary goal [BPS10].

Regarding the distortion characteristic, conformal maps are more useful for general shape and pattern analysis. Mathematically conformal maps always exist, are unique, and locally Euclidean. Möbius transformations allow for normalization, zooming, and focusing inside the generated map. This can be used to overcome the problem of the typically highly distorted appearance around borders in the target domain as the point of focus can be changed [HS09].

Equiareal flattening techniques should be preferred if accurate modality sampling and statistical sensitivity is critical, e.g. if studying the neuronal density, cortical functional activation extent, or cortical thickness [ZHGH11]. The same applies for marking and tracking of cortical landmark curves which is easier to perform when deeply burried Gyri and Sulci are more evenly spread out in area-preserving visualizations [SZS*13]. Especially in case of mapping a cortical hemisphere to the unit disk. Anatomical structures tend to concentrate in the center, whereas large area distortions occur closer to the border of the disk.

Without cuts, isometric mappings are usually only applicable to smaller regions of interest, otherwise, larger distortions are intro-

duced. Beside the often approximated Euclidean shortest path distances, the exact geodesic distance has to be considered, otherwise the mapping is error-prone [BPS10].

Furthermore, mapping to a sphere is common and seems intuitive for brain data, however, it can introduce significant distortions in the parameter domain [FSD07, WZG*10]. Landmark cuts can help to reduce distortion in the mapping to all types of target domains, yet, they separate spatially neighboring points.

With respect to the creation of application-specific visualizations, using these parameterization algorithms, we have to consider that the brain is a highly convoluted surface. Although the brain's Sulci and Gyri are recognizable in the flattened representation, the self-similar appearance renders the user's orientation difficult. However, flat maps, such as rectangles or circles, show the entire pattern in a single view. On the other hand, mapping to the sphere has the advantage that it respects the general surface topology of the brain. Additionally overlaid information such as landmarks, cortical activity, or atlases help to associate features of the brain's geometry to the underlying data which the visualization wants to convey.

6. Application: Tumor Maps

In contrast to the other application sections in this STAR, which are focusing on a specific organ, this section focuses on anomalies, i.e., tumors. For these, a few flattening techniques have been proposed in the past, which are discussed in this section.

6.1. Tasks and Requirements

Various interventional therapies aim at destroying a malignant tumor (primary tumor or metastasis) by applying heat. These therapies include *laser-induced interstitial thermotherapy* (LITT), *radio frequency ablation* (RFA), and *microwave ablation*. Substantial clinical experiences exist to treat liver, kidney, and lung tumors. The basic approach is the same: physicians have to evaluate whether a tumor is eligible for interventional treatment based on the tumor size and location. If this is the case, they plan a trajectory (entry point on the skin and target point close to the tumor center) where the needle of an applicator should be inserted to deliver thermal energy. These therapies are restricted to small to medium-sized tumors since larger tumors cannot be fully destroyed. Tumors too close to larger branches of vascular structures are critical since these vascular structures should be preserved and also since they lead to a cooling effect that counteracts the heating process of the intervention. Whether or not a sufficient destruction of a tumor can be achieved with an interventional treatment is difficult to assess in some cases. Therefore, simulations are carried out that consider tissue-specific heat properties and deliver for each voxel the estimated temperature as an indicator for the likelihood of tumor control.

6.2. Techniques

Tumor maps [RWS*10] summarize the spatial information of the simulation along with the morphology of the tumor and its safety

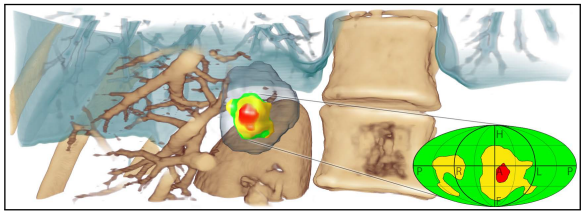

(a) Rieder et al. [RWS*10]

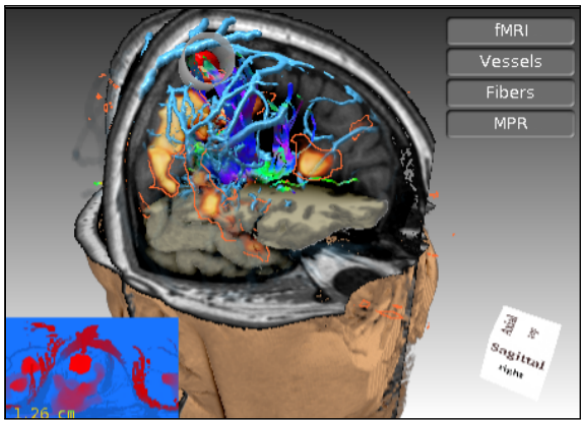

(b) Diepenbrock et al. [DPL*10]

Figure 28: *Two different examples of tumor maps. Rieder et al. [RWS*10] use a more illustrative color coding (a), while Diepenbrock et al. [DPL*10] directly project structures at risk onto the map (b). (From [RWS*10] and [DPL*10])*

margin to support the treatment planning process. They discriminate three portions of tissue: tumor tissue inside the coagulation safety margin (shown in green), tumor tissue within the coagulation region but outside the safety margin (shown in yellow) and tumor tissue outside of the coagulation region, i.e. tumor tissue that will *not* be destroyed (shown in red). According to this scheme, the tumor surface is color-coded simultaneously in a 3D visualization and a 2D map projection that shows the entire tumor surface, see Figure 28(b). In an interactive setting, the planned needle position may be changed when the tumor map contains yellow or even red portions until an appropriate needle placement is found.

The specific mapping of the tumor map is the Mollweide projection which is area-preserving. This cylindrical mapping is based on mapping longitude and latitude values to a rectangular coordinate system. The usefulness of this mapping depends on the synchronization with the 3D visualization that provides the necessary anatomical context. Another essential set of cues are labels in the map indicating, e.g. the head and foot direction.

A similar approach has been presented by Diepenbrock et al. [DPL*10]. They focus on the generation of maps depicting brain tumors. The main goal of their approach is to convey vicinity to structures at risk. To do so, they use a ray-based approach, in which rays are cast from the tumor center by sampling spherical coordinates. To obtain the distance to the structures at risk, these are projected into the plane by means of the samples, and

depth encoded through pseudo-chromadepth coloring [RSH06]. Figure 28(b) shows an example of such a flattening.

6.3. Usage Guidelines

Since only very few techniques have been presented in this area, it is difficult to formulate specific guidelines. Nevertheless, in the reviewed work, we have found that the representation of the anatomical context seems to be even more crucial than in the other application scenarios discussed. We believe that this is the case, since in contrast to organs, for tumors the overall structure and location are in general unknown, which makes context more essential. Tumor risk maps should convey the tumor's shape and the spatial surroundings relevant for intervention or radiation treatment planning. Distortions that affect the perception of these distances need to be minimized. In particular, the vicinity to vascular structures with a minimum diameter must be (roughly) preserved. If simulations are performed, e.g. simulation of radiation or temperature simulations for RFA, an overlay of the major anatomical structures and the scalar simulation results will be helpful. Color selection is challenging in these cases. A red-yellow-green scheme for anatomical structures that are safe or at moderate or high risk is typically used. However, when simulation results should be overlaid, this needs to be adapted. An option is to use isolines to convey the simulation results. The authors use labels, depth encoding, and linked 3D visualizations to provide this context [RWS*10].

7. Application: Bone Flattening

Many of the approaches tailored for the flattening of bone structures show similarities to curved planar reformations [KFW*02], since the mapping of elongated structures, relevant for many bones, can benefit from this approach. In this section we describe those flattening techniques which are specifically developed for bone structures.

7.1. Tasks and Requirements

When flattening bone structures, usually one of the following two tasks needs to be fulfilled. The first task deals with the assessment of bone ruptures. This is especially relevant in emergency units, where trauma care plays an important role. Consequently, several of the reviewed bone flattening techniques have been evaluated in this context, e.g., [RLT*15]. The second most frequently occurring task in the context of bone flattening is the detection of metastases, as they can occur everywhere. Therefore, an overview of suspicious locations is very important to carry out further actions and a high accuracy in their detection is indispensable. Furthermore, the comparison of single or multiple bones. Here, the bones to be investigated are flattened to compare them by means of juxtaposition or overlap. Especially when dealing with cohort studies, an overlap can also be used to integrate many data points of a longitudinal study into a singe representation to compute difference metrics.

7.2. Techniques

Vrtovec et al. [VLP05, VOG*06, VOG*07, Vrt15] present a spine-based coordinate system to provide planar cross-sectional images following the spine. This system is defined by a curve that runs

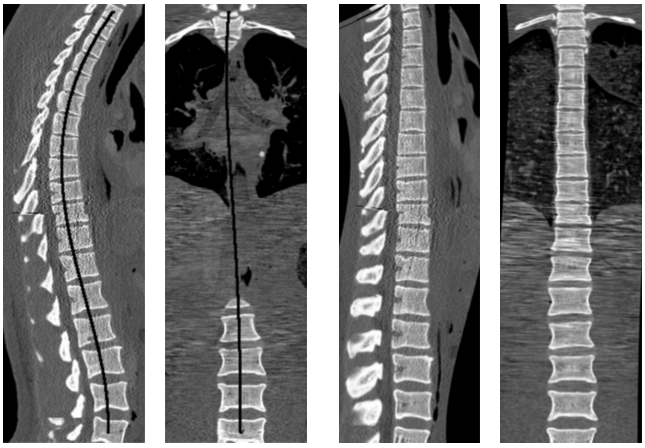

Figure 29: *Coronal and sagittal slice views. (a)-(b) show conventional image-based slice view, whereas (c)-(d) present spine-based slices. The projection of the spinal centerline is shown in the image-based slice views in black. (From [VLP05])*

through the center of the thickest part of the vertebrae — determined by a distance transform and an optimization of the curve parameters. Along this curve, a new local coordinate system is defined by projecting the Cartesian x-axis and y-axis into the cross-section perpendicular to the curve. Then, intensity-based symmetry of the vertebra is used to rearrange this plane in order to coincide with the symmetry axis. This ensures that the coordinate system reflects the spine as well as vertebrae in a sufficient quality. The conventional coronal, sagittal, and axial slice view can be directly translated to the spine-based coordinate system, leading to anatomically adapted views that resemble either a projected or straightened CPR as depicted in Figure 29(c)-(d). Neither the straightened nor the projected slice views preserve isometry or conformity.

As discussed in the related work section of this state-of-the-art report, Saroul [Sar06] discusses several flattening techniques for anatomical structures such as **rib unfolding**. Among those are many techniques applicable to or tailored towards bone structures. An example frequently found in his thesis is the flattening of the human jaw, in which the central jaw's surface is embedded into the image plane. Recently, several authors evaluate the effect of rib unfolding with respect to diagnostic accuracy [GPH*16, KMD*17, DSE*17]. Ringl et al. for instance have applied rib unfolding in trauma care and propose an efficient unfolding algorithm to allow for a fast assessment of rib fractures [RLT*15]. Based on CT data of 220 trauma cases, they compare the investigated diagnosis based on rib unfolding as opposed to standard MPR techniques. To realize the used unfolding, the center lines are computed for all ribs. On this basis, ribs are matched to a template model, which is used for the unfolding. The authors find that rib unfolding is not only resulting in a more accurate analysis, i.e., more fractures have been detected, but also in a reduced time needed for diagnosis.

Kok et al. propose a reformation technique to convey changes in multiple CT scans of mice [KBH*10]. Their approach deals with

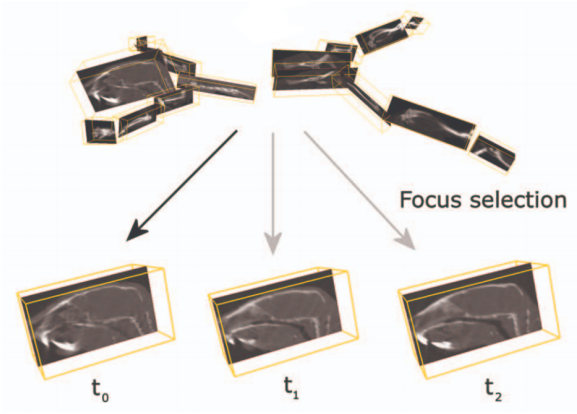

Figure 30: *The articulated planar reformation (APR), allows for an interactive unfolding of whole-body small animal CT scans, which reduces occlusions and helps to emphasize the current object of interest, when comparing several scans (Adapted from [KBH*10])*

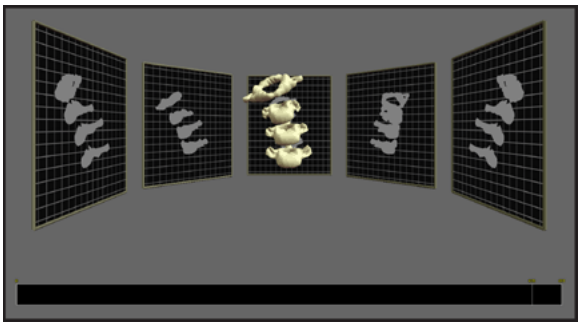

Figure 31: *Different projections are used to support the assessment of kinetic motion data. The example shows the application to a spine acquired in a kinematic study. (From [CKHS*12])*

two main issues when analyzing multiple whole-body small animal CT scans: the varying posture and occlusions between different parts of interest. To deal with these challenges, they propose **articulated planar reformation**, which maps given CT scans to an atlas to generate an interactive reformation visualization. After the atlas is embedded into a CT scan, the subvolumes corresponding to the individual extremities are extracted and arranged based on the current region of interest (see Figure 30).

Coffey et al. compare different approaches for visualizing motion data, acquired in kinematic studies [CKHS*12]. One design, the so-called *Static Space*, Interactive Time design is applied to data from a spinal kinematics study, whereby different projection planes are used for a better comparison. In contrast to other bone flattening techniques, this visualization does not involve a reformation step, but rather perspective projections from different views, see Figure 31.

Klemm et al. focuse on the analysis of image-based cohort study data, in which they facilitate the comparative anaysis of the

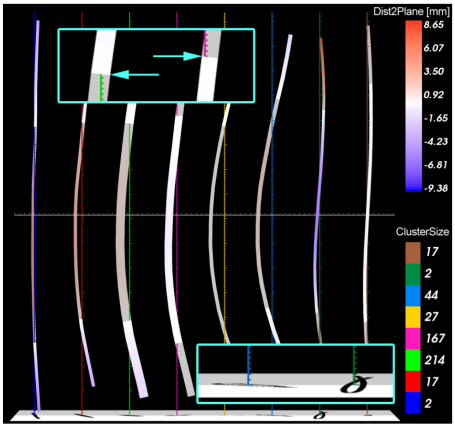

Figure 32: *Klemm et al. extract centerlines from splines segmented in cohort imaging data. Thus, several clusters can be identified, and splines can be overlapped to support comparison. (From [KLR*13])*

spine [KLR*13]. Specifically, they are interested in the visualization and analysis of lumbar spine canal variability within a cohort data set. To enable the proposed flattening, they exploit a model-based segmentation of the spine, identify the lumbar canal, and derive its centerline. Based on such extracted centerlines, they perform an Agglomerative Hierarchical Clustering in order to obtain groups of similar canal shapes. Each cluster is then visualized by means of a representative, which can be considered a special form of overlap visualization (see Figure 32).

Kretschmer et al. [KST*14] describe a reformation technique, referred to as anatomy-driven reformation (ADR) that reformats a volume along a structure- or object-specific surface, as demonstrated in Figure 33. By using an as-rigid-as-possible (ARAP) mapping, angle and length measurements are preserved (local rigidity). In order to view not only the flattened surface, but also its 3D vicinity or surrounding volume, it is offset in positive and negative normal direction. The volume spanned between these three surfaces is again parameterized ARAP and flattened, offering a volumetric reformation. Since flattening a surface does not adapt the distortions to specific regions, an importance map can be defined to do so. This importance-driven reformation adjusts the mapping weights in order to minimize distortion in the important areas.

De Leener et al. [DMD*17] describe an approach for topology-preserving straightening of the spinal cord. They approximate the spinal cord with a non-uniform rational B-spline (NURBS) curve and find for every voxel the equidistantly sampled point with minimal distance to the voxel itself. Then, the voxel is projected into the plane perpendicular to the centerline curve spanned by the closest sampled centerline point and the tangent vector of the centerline in this point. By knowing the correspondences of the centerline points and their local coordinate systems along the curved and the straightened space, the transformation of a voxel is well-defined. This mapping does not preserve isometry, but conformity.

Martinke et al. [MPG*17] describe a rib unfolding approach that uses ray-casting to compute a cross-sectional model that adapt to

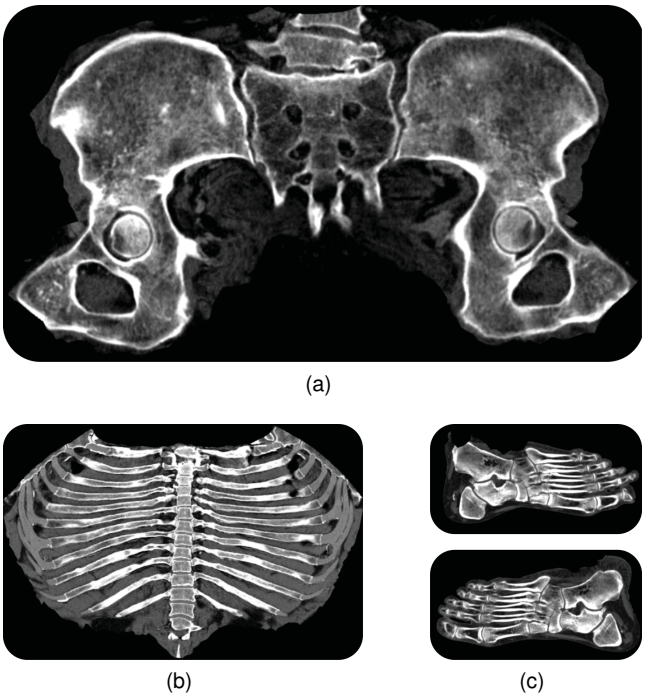

Figure 33: *Examples of ADR generated by considering the underlying anatomical structure. (a) shows a flattened pelvis, (b) a flattened rib cage, and (c) flattened feet. (Adapted from [KST*14])*

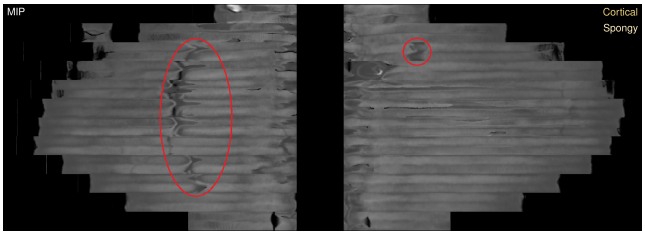

Figure 34: *An exemplar case with several complete rib fractures (red circles). The cortical and spongy bone layers of all ribs are unfolded and aggregated into a single image using maximum intensity projection (MIP). Since each rib is flattened to the same height, they can be arranged in a standardized layout. (From [MPG*17])*

the shape of the ribs. By sampling these rays until they leave the ribs, several shape-adaptive slices can be unfolded and aggregated using, e.g., maximum intensity projection (MIP) as shown in Figure 34 of the cortical and spongy bone layers. These slices are all scaled to a rectangle of fixed extent, which makes it possible to arrange all ribs in a standardized layout, but with the price of losing isometry. Certain types of bone fractures or lesions affect only specific layers, either the cortical or spongy bone layer. To differentiate and localize such fractures, the described approach allows physicians to inspect only one of these two layers separated or both together in a single image.

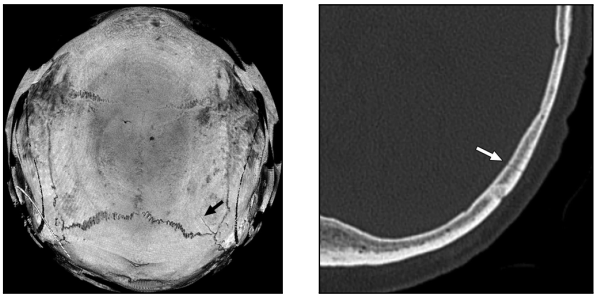

Figure 35: *Curved thin maximum intensity projection applied to a cranial CT scan (a). The comparable traverse slice (b) does not as clearly show the fracture. In each image fractures are indicated by the arrows. (From [RSS*10])*

Besides these approaches, also some work has been done on unfolding cranial data. Ringl and colleagues have been working on algorithms for skull unfolding based on CT data [RSS*10]. By using their approach, which is based on curved maximum intensity projections (MIPs), it becomes possible to embed such data into the plane and thus assess head fractures using a single image only (see Figure 35(a)). To evaluate their technique, the authors compared its application to the assessment of transverse sections (see Figure 35(b)). Their findings show that the curved MIPs enable a significantly higher fracture detection rate, as compared to the transverse slices.

7.3. Usage Guidelines

When dealing with skeletal imaging data, it is essential to consider the task at hand as well as the structures represented by the data, when deciding which flattening technique to use. With respect to the data we distinguish two main groups. First, the data where the focus lies on a single bone structure, such as for instance the rib cage or the jaw. In such cases it is important that the structure of interest can be examined from all sides within a single flattening. Consequently, such flattenings have bad preservation properties, as the flattening goes hand in hand with a deformation. The second group contains all those acquisitions where several structures in terms of bones shall be investigated. In such cases the flattening techniques can benefit from the empty space in between individual bones, and lay them out, such that all bones are visible. Accordingly, better preservation properties can be expected. While entire skeletons clearly fall into this category, the rib cage has properties of both groups.

With respect to the task, the situation is unfortunately unclear. When for instance trying to spot fractures, this works well on single bones. In contrast, when working with entire skeletons, often parts of the individual bones are occluded. Consequently, task and data acquisition cannot be taken into account independently.

8. Guidelines

We have presented several medical visualization domains where flattening algorithms are heavily applied. Each of these sections has their own task-related guidelines, however, some general rules and suggestions can be formulated. To provide a structure for such guidelines, we separate them into data handling and processing, comparison, visualization and presentation, and distortion handling guidelines.

Data handling and processing. One of the first decisions to be made is the general type of preservation, either topological or geometrical. Topological structures are usually more important for pattern analysis and visualization tasks, and conformal parameterizations are to be preferred in such cases, as the viewer is not particularly interested in specific data points or values, but rather in scene comprehension and exploration. Such a preservation of topological features is for instance crucial for surface registration or abnormality detection. Thus, it is especially applicable when comparing several data sets.

For quantitative analysis, it should instead be focused on geometric properties of the parameterization. Equiareal flattening techniques should be preferred where accurate modality sampling and statistical sensitivity is critical. Quasi-isometric mappings are usually more suitable for smaller regions of interest, otherwise, larger distortions are introduced. Besides the often approximated Euclidean shortest path distances in isometric parameterizations, the exact geodesic distance has to be considered, otherwise the mapping is error-prone [BPS10].

If a separation of neighboring surface points is acceptable for an application, landmark cuts help to reduce distortion in the mapping to all types of target domains. Furthermore, constraining the flattening process to a region of interest can simplify the mapping problem and reduce the computational overhead. However, this is difficult for closed genus zero surfaces, such as the sphere, if the topology has to be preserved.

Data comparison. A superimposed comparison between two flattening approaches is difficult as they usually generate highly different results. The cause is that flattening techniques are often based on optimization algorithms, therefore, their results are usually ambiguous. Landmark registration is one attempt to solve this problem, but sill does not guarantee a comparable result. This general problem was especially pointed out and criticized by Balasubramanian et al. [BPS10] for brain surface parameterizations, but applies to all fields of application discussed in this paper.

Data visualization and presentation. To address the problem of spatial context preservation and to avoid potential *conformation bias*, annotations and further anatomical indicators can be utilized, the VBEP by Teermeer et al. [TBB*07] or placenta maps from Miao et al. [MMK*17]. For detailed data exploration scenarios, a visual combination of the 3D and 2D flattened surface is suggested. This setup provides a spatial correlation between both depictions, 2D could be used as an overview to highlight regions of interest, which can then be inspected in detail in 3D. To communicate multivariate data, additionally overlaid information such as landmarks, atlases, or labels help to associate geometric features with the underlying information. An example would be the display of fMRI data together with surfaces extracted from MRI scans.

To enable physicians to read visualizations more easily, abstraction is often used as a tool to present complex data. We believe that flattening techniques are popular since they exploit such an abstraction. However, it shall be pointed out the degree of abstraction will correlate with the amount of training required. For visualizations not frequently used the degree of abstraction should be smaller compared to those visualizations a physician is exposed to on a daily basis.

Distortion handling. To reduce the overall amount of distortion, one strategy is to apply conformal and equiareal algorithms successively [ZHGH11]. However, this inherits the problem that the initial preservation characteristic can be completely lost if no countermeasures are carried out.

To visualize distortion artifacts of the parameterization, heat maps are a common visualization technique. Furthermore, uncertainty visualization of inferred parameters is used to communicate data and raise awareness of the user [RWS*10, RKSH11, Bre12].

A general problem of CPR-based flattening methods is that such techniques produce depth discontinuities, which negatively influence the diagnosis process of vessel diseases. Therefore, Kretchmer et al. [KPS14] presented a bilateral filtering approach that removes such depth discontinuities. For filtering, constraints are set to ensure that the depth map still passes through the vessel centerlines. Otherwise, the vessel topology is changed, which is not desired.

However, existing distortions in flattening methods have consequences for their application in diagnostic scenarios. In clinical routine, flattening techniques are never independently used, always in combination with conventional, well-established visualization techniques such as the slice views. Projections are mostly utilized to provide an overview of the essential aspects while being linked with other representations for a more detailed diagnosis. Regarding the diagnosis of vascular diseases, the studies of Schernthaner et al. [SWM*15] and Portugaller et al. [PSH*04] show that axial slice views still have to be used.

9. Conclusions

We have discussed and classified flattening techniques used in medical visualization. To enable users and visualization experts to assess usage scenarios of the reviewed techniques, we have developed a coding system based on three property groups: Data Input, Transferability, and Preservation. Within these groups, we could identify in total seven axes which form the basis of our comparative literature review. To structure this STAR, we have discussed the techniques with respect to their application cases, starting with the cardiovascular system, continuing with colon unfolding and brain flattening, and arriving at tumor maps and finally bone flattening techniques. All reviewed techniques have been discussed based on our coding scheme.

10. Future Challenges

One future challenge of flattening surfaces is the investigation of a *thick slab* instead of a single thin slice. Concerning flattening of

vascular structures, Kanitsar et al. [KFW*02] and Cai et al. [Cai07] use a slab for rendering thick CPRs. Zeng et al. [ZMKG11] consider the volumetric colon wall, and in the brain flattening domain Wang et al. [WGC*04b] use harmonic volumetric mapping and Khosravi and Soltanian-Zadeh [KSZ14] a multi-surface approach. Although these papers provide interesting results, problems could be caused by high-intensity structures, e.g. calcification blending over the vessel lumen.

Most of the presented techniques are tailored towards a quite specific problem to be solved. This lack of generalizability reflects also in our classification table (Table 1)—the reproducibility is nearly always higher rated than the generalizability. The investigation of approaches which can handle more complicated topologies could compensate for defective segmentation results. Otherwise, more robust reconstruction algorithms or automatic repairing methods have to be applied in preprocessing steps.

Kreiser and Ropinski [KR16] formulated the following two statements of what could also be considered in future work concerning medical projection and parameterization techniques.

Medical projection techniques which currently do not implement any preservation characteristic, such as the Volumetric Bulls Eye Plot [TBB*07] or Aneurism Maps [NGB*09], could be extended to do so. However, it has to be considered that an enforced preservation characteristic does not automatically enhance any type of flattened visualization, especially if quantitative geometric measures are not highly relevant.

Further attention should also be paid to techniques considering shape [MK16], context [KSW06, MC10], or mass [ZYHT07] preservation. Especially context-preservation in complex environments benefits the user when focusing on a region of interest while the overall picture is still important. Another user-centered orientation would be the development of data-aware approaches which automatically optimize the visual representation with respect to a given task.

Acknowledgement

This work was partially funded by the Deutsche Forschungsgemeinschaft (DFG) under grants RO 3408/2-1 (Prolint) and RO 3408/3-1 (Inviwo). The authors thank the Ulm University Center for Translational Imaging MoMAN for its support. Some of the described techniques have been realized in the Inviwo visualization framework (www.inviwo.org).

Biographies

Julian Kreiser is a research associate at the Visual Computing Group at Ulm University, Germany. Having a background in computer vision technology, his current focus is machine vision aided medical visualization in laparoscopic environments.

Monique Meuschke is a Doctoral Research Fellow at the Computer Science Department and part of the research campus STIMULATE at the University of Magdeburg, Germany. In 2015, she received a master in Computational Visualistics. Her research is focused on the exploration and analysis of cerebral and cardiac blood flow data.

Gabriel Mistelbauer is a postdoctoral researcher at the Otto-von-Guericke University Magdeburg, Germany since 2016. Before, he was a postdoctoral researcher at TU Wien, Austria, where he received a Ph.D. (2013) in computer science and a Master's degree (2010) in visual computing. His research mainly focuses on medical visualization, especially on the visual analysis of blood vessels and therapy planning.

Bernhard Preim is a professor for visualization at the University of Magdeburg. He received a PhD and a Masters in computer science from the University of Magdeburg, and post-doctoral lecture qualification (Habilitation) at the University of Bremen. His research is focused on medical applications targeting diagnostic and treatment planning processes as well as medical education.

Timo Ropinski is a professor at Ulm University, where he is heading the Visual Computing Group. Before moving to Ulm he was Professor in Interactive Visualization at Linköping University in Sweden, where he was heading the Scientific Visualization Group. He has received his Ph.D. in computer science in 2004 from the University of Münster, where he has also completed his Habilitation in 2009. His current research interests in visualization have a strong focus on biomedical applications.

References

[ADGP*15] AUZIAS G., DE GUIO F., PEPE A., ROUSSEAU F., MANGIN J.-F., GIRARD N., LEFÈVRE J., COULON O.: Model-driven parameterization of fetal cortical surfaces. In *Proc. of IEEE Symposium on Biomedical Imaging* (2015), pp. 1260–1263. 18

[AH11] ANGELELLI P., HAUSER H.: Straightening tubular flow for side-by-side visualization. *IEEE Transactions on Visualization and Computer Graphics 17*, 12 (2011), 2063–2070. 4, 10, 11

[AHTK99a] ANGENENT S., HAKER S., TANNENBAUM A., KIKINIS R.: Conformal geometry and brain flattening. In *Proc. of Medical Image Computing and Computer-Assisted Intervention* (1999), pp. 271–278. 4, 15, 18

[AHTK99b] ANGENENT S., HAKER S., TANNENBAUM A., KIKINIS R.: On the laplace-beltrami operator and brain surface flattening. *IEEE Transactions on Medical Imaging 18*, 8 (1999), 700–711. 4, 9, 15, 16

[ALLT*13] AUZIAS G., LEFÈVRE J., LE TROTER A., FISCHER C., PERROT M., RÉGIS J., COULON O.: Model-driven harmonic parameterization of the cortical surface: HIP-HOP. *IEEE Transactions on Medical Imaging 32*, 5 (2013), 873–887. 2, 4, 18

[AMB*13] AUZINGER T., MISTELBAUER G., BACLIJA I., SCHERNTHANER R., KÖCHL A., WIMMER M., GRÖLLER M. E., BRUCKNER S.: Vessel visualization using curved surface reformation. *IEEE Transactions on Visualization and Computer Graphics 19*, 12 (2013), 2858–2867. 4, 11

[AMRB98] ACHENBACH S., MOSHAGE W., ROPERS D., BACHMANN K.: Curved multiplanar reconstructions for the evaluation of contrast-enhanced electron beam CT of the coronary arteries. *American Journal of Roentgenology 170*, 4 (1998), 895–899. 7

[BFLC04] BÜHLER K., FELKEL P., LA CRUZ A.: Geometric methods for vessel visualization and quantification–a survey. In *Geometric modeling for scientific visualization*. Springer, 2004, pp. 399–419. 2

[BGP*11] BORKIN M. A., GAJOS K. Z., PETERS A., MITSOURAS D., MELCHIONNA S., RYBICKI F. J., ANDHANSPETER PFISTER C. L. F.: Evaluation of artery visualizations for heart disease diagnosis. *IEEE Transactions on Visualization and Computer Graphics 17*, 12 (2011), 2479–2488. 4, 10

[BPS10] BALASUBRAMANIAN M., POLIMENI J. R., SCHWARTZ E. L.: Near-isometric flattening of brain surfaces. *NeuroImage 51*, 2 (2010), 694–703. 4, 17, 18, 19, 23

[Bre12] BRECHEISEN R.: *Visualization of uncertainty in fiber tracking based on diffusion tensor imaging*. PhD thesis, PhD thesis, Technische Universiteit Eindhoven, 2012. Department of Biomedical Engineering, 2012. 23

[BWKG01] BARTROLÍ A. V., WEGENKITTL R., KÖNIG A., GRÖLLER E.: Nonlinear virtual colon unfolding. In *Proc. of IEEE Visualization* (2001), pp. 411–420. 4, 13

[Cai07] CAI W.: 3D planar reformation of vascular central axis surface with biconvex slab. *Computerized Medical Imaging and Graphics 31*, 7 (2007), 570–576. 4, 9, 24

[CES*08] CHIU B., EGGER M., SPENCE D. J., PARRAGA G., FENSTER A.: Area-preserving flattening maps of 3D ultrasound carotid arteries images. *Medical Image Analysis 12*, 6 (2008), 676–688. 4, 10

[CKHS*12] COFFEY D., KORSAKOV F., HAGH-SHENAS H., THORSON L., ELLINGSON A., NUCKLEY D., KEEFE D. F.: Visualizing motion data in virtual reality: Understanding the roles of animation, interaction, and static presentation. *Computer Graphics Forum 31*, 3pt3 (2012), 1215–1224. 4, 21

[CLL15] CHOI P. T., LAM K. C., LUI L. M.: FLASH: Fast landmark aligned spherical harmonic parameterization for genus-0 closed brain surfaces. *SIAM Journal on Imaging Sciences 8*, 1 (2015), 67–94. 4, 18

[CRM*10] CLOUCHOUX C., RIVIÈRE D., MANGIN J.-F., OPERTO G., RÉGIS J., COULON O.: Model-driven parameterization of the cortical surface for localization and inter-subject matching. *NeuroImage 50*, 2 (2010), 552–566. 18

[CWD*02] CERQUEIRA M. D., WEISSMAN N. J., DILSIZIAN V., JACOBS A. K., KAUL S., LASKEY W. K., PENNELL D. J., RUMBERGER J. A., RYAN T., VERANI M. S.: Standardized myocardial segmentation and nomenclature for tomographic imaging of the heart. *Circulation 105*, 4 (2002), 539–542. 4, 5

[CWW*16] CUI H. F., WANG D. S., WAN M., ZHANG J. M., ZHAO X. D., TAN S. Y., WONG A. S. L., TAN R. S., HUANG W. M., XIONG W., DUAN Y. P., ZHOU J. Y., CHI Y. L., ZHONG L.: Quantification of coronary artery cross section lumen area and area stenosis with 3D centerline-centric straightening. In *Proc. of Innovation in Biomedical Engineering and Life Sciences* (2016), vol. 56, pp. 306–309. 4, 11

[DHS*13] DIEPENBROCK S., HERMANN S., SCHÄFERS M., KUHLMANN M., HINRICHS K. H.: Comparative visualization of tracer uptake in in vivo small animal PET/CT imaging of the carotid arteries. *Computer Graphics Forum 32*, 3 (2013), 241–250. 4, 11

[DMD*17] DE LEENER B., MANGEAT G., DUPONT S., MARTIN A. R., CALLOT V., STIKOV N., FEHLINGS M. G., COHEN-ADAD J.: Topologically preserving straightening of spinal cord MRI. *Journal of Magnetic Resonance Imaging 46*, 4 (2017), 1209–1219. 4, 21

[DPL*10] DIEPENBROCK S., PRASSNI J.-S., LINDEMANN F., BOTHE H.-W., ROPINSKI T.: Pre-operative planning of brain tumor resections. *IEEE Visualization Contest* (2010). 4, 19

[DSE*17] DANKERL P., SEUSS H., ELLMANN S., CAVALLARO A., UDER M., HAMMON M.: Evaluation of rib fractures on a single-in-plane image reformation of the rib cage in CT examinations. *Academic Radiology 24*, 2 (2017), 153–159. 20

[DVEA*96] DRURY H. A., VAN ESSEN D. C., ANDERSON C. H., LEE C. W., COOGAN T. A., LEWIS J. W.: Computerized mappings of the cerebral cortex: a multiresolution flattening method and a surface-based coordinate system. *Journal of Cognitive Neuroscience 8*, 1 (1996), 1–28. 16, 17

[FH02] FLOATER M., HORMANN K.: Parameterization of triangulations and unorganized points. In *Tutorials on Multiresolution in Geometric Modelling*. Springer, 2002, pp. 287–316. 2

[FH05] FLOATER M. S., HORMANN K.: Surface parameterization: a tutorial and survey. In *Advances in multiresolution for geometric modelling*. Springer, 2005, pp. 157–186. 2

[Fis12] FISCHL B.: Freesurfer. *Neuroimage 62*, 2 (2012), 774–781. 2

[FJS*09] FÖLL D., JUNG B., STAEHLE F., SCHILLI E., BODE C., HENNIG J., MARKL M.: Visualization of multidirectional regional left ventricular dynamics by high-temporal-resolution tissue phase mapping. *Journal of Magnetic Resonance Imaging 29*, 5 (2009), 1043–1052. 6

[Flo97] FLOATER M. S.: Parametrization and smooth approximation of surface triangulations. *Computer Aided Geometric Design 14*, 3 (1997), 231–250. 16

[Flo03] FLOATER M. S.: Mean value coordinates. *Computer Aided Geometric Design 20*, 1 (2003), 19–27. 12, 16

[FSD99] FISCHL B., SERENO M. I., DALE A. M.: Cortical surface-based analysis: II: inflation, flattening, and a surface-based coordinate system. *Neuroimage 9*, 2 (1999), 195–207. 16

[FSD07] FRIEDEL I., SCHRÖDER P., DESBRUN M.: Unconstrained spherical parameterization. *Journal of Graphics Tools 12*, 1 (2007), 17–26. 19

[GAW*11] GLEICHER M., ALBERS D., WALKER R., JUSUFI I., HANSEN C. D., ROBERTS J. C.: Visual comparison for information visualization. *IEEE Information Visualization 10*, 4 (2011), 289–309. 1

[Goe00] GOEBEL R.: A fast automated method for flattening cortical surfaces. *NeuroImage 11*, 5 (2000), 680. 4, 15

[GPH*16] GLEMSER P. A., PFLEIDERER M., HEGER A., TREMPER J., KRAUSKOPF A., SCHLEMMER H.-P., YEN K., SIMONS D.: New bone post-processing tools in forensic imaging: a multi-reader feasibility study to evaluate detection time and diagnostic accuracy in rib fracture assessment. *International Journal of Legal Medicine* (2016), 1–8. 20

[GSK*12] GOUBERGRITS L., SCHALLER J., KERTZSCHER U., VAN DEN BRUCK N., POETHKOW K., PETZ C., HEGE H. C., SPULER A.: Statistical wall shear stress maps of ruptured and unruptured middle cerebral artery aneurysms. *Journal of the Royal Society Interface 9*, 69 (2012), 677–688. 4, 7, 12

[GSZ*13] GURIJALA K. C., SHI R., ZENG W., GU X., KAUFMAN A.: Colon flattening using heat diffusion riemannian metric. *IEEE Transactions on Visualization and Computer Graphics 19*, 12 (2013), 2848–2857. 4, 14

[GWC*04] GU X., WANG Y., CHAN T. F., THOMPSON P. M., YAU S.-T.: Genus zero surface conformal mapping and its application to brain surface mapping. *IEEE Transactions on Medical Imaging 23*, 8 (2004), 949–958. 4, 15, 16, 17

[HATK00a] HAKER S., ANGENENT S., TANNENBAUM A., KIKINIS R.: Non-distorting flattening for virtual colonoscopy. In *Proc. of Medical Image Computing and Computer-Assisted Intervention* (2000), Delp S. L., DiGoia A. M., Jaramaz B., (Eds.), pp. 358–366. 4, 13

[HATK00b] HAKER S., ANGENENT S., TANNENBAUM A., KIKINIS R.: Nondistorting flattening maps and the 3D visualization of colon CT images. *IEEE Transactions on Medical Imaging 19*, 7 (2000), 665–670. 4, 13

[HBM*15] HOFMAN A., BRUSSELLE G. G., MURAD S. D., VAN DUIJN C. M., FRANCO O. H., GOEDEGEBURE A., IKRAM M. A., KLAVER C. C., NIJSTEN T. E., PEETERS R. P., ET AL.: The rotterdam study: 2016 objectives and design update. *European Journal of Epidemiology 30*, 8 (2015), 661–708. 1

[HBS*99] HURDAL M. K., BOWERS P. L., STEPHENSON K., DE WITT L. S., REHM K., SCHAPER K., ROTTENBERG D. A.: Quasi-conformally flat mapping the human cerebellum. In *Proc. of Medical Image Computing and Computer-Assisted Intervention* (1999), pp. 279–286. 4, 15

[HDL*01] HE S., DAI R., LU B., CAO C., BAI H., JING B.: Medial axis reformation: A new visualization method for ct angiography. *Academic Radiology 8*, 8 (2001), 726–733. 4, 8

[HGQ*06] HONG W., GU X., QIU F., JIN M., KAUFMAN A.: Conformal virtual colon flattening. In *Proc. of ACM Symposium on Solid and Physical Modeling* (2006), pp. 85–93. 4, 13

[HPR*08] HINDS O., POLIMENI J. R., RAJENDRAN N., BALASUBRAMANIAN M., WALD L. L., AUGUSTINACK J. C., WIGGINS G., ROSAS H. D., FISCHL B., SCHWARTZ E. L.: The intrinsic shape of human and macaque primary visual cortex. *Cerebral Cortex 18*, 11 (2008), 2586–2595. 17

[HS04] HURDAL M. K., STEPHENSON K.: Cortical cartography using the discrete conformal approach of circle packings. *NeuroImage 23* (2004), 119–128. 4, 15

[HS09] HURDAL M. K., STEPHENSON K.: Discrete conformal methods for cortical brain flattening. *Neuroimage 45*, 1 (2009), 86–98. 4, 15, 18

[HSS*99] HURDAL M. K., SUMNERS D., STEPHENSON K., BOWERS P. L., ROTTENBERG D. A.: Circlepack: software for creating quasi-conformal flat maps of the brain. *NeuroImage 9* (1999), 250–250. 2, 16

[JHS*05] JU L., HURDAL M. K., STERN J., REHM K., SCHAPER K., ROTTENBERG D.: Quantitative evaluation of three cortical surface flattening methods. *NeuroImage 28*, 4 (2005), 869–880. 16

[JSR*04] JU L., STERN J., REHM K., SCHAPER K., HURDAL M., ROTTENBERG D.: Cortical surface flattening using least square conformal mapping with minimal metric distortion. In *Proc. of IEEE Symposium on Biomedical Imaging* (2004), pp. 77–80. 4, 16

[JSTL04] JOSHI A. A., SHATTUCK D. W., THOMPSON P. M., LEAHY R. M.: Cortical surface parameterization by p-harmonic energy minimization. In *Proc. of IEEE Symposium on Biomedical Imaging* (2004), pp. 428–431. 4, 15

[Kan04] KANITSAR A.: *Curved Planar Reformation for Vessel Visualization*. PhD thesis, TU Wien, 2004. URL: http://diglib.eg.org/handle/10.2312/8168. 7, 8

[KBH*10] KOK P., BAIKER M., HENDRIKS E. A., POST F. H., DIJKSTRA J., LOWIK C. W., LELIEVELDT B. P., BOTHA C. P.: Articulated planar reformation for change visualization in small animal imaging. *IEEE Transactions on Visualization and Computer Graphics 16*, 6 (2010), 1396–1404. 4, 20, 21

[KFW*02] KANITSAR A., FLEISCHMANN D., WEGENKITTL R., FELKEL P., GRÖLLER M. E.: CPR – curved planar reformation. In *Proc. of IEEE Visualization* (2002), pp. 37–44. 4, 7, 8, 9, 20, 24

[KFWG06] KANITSAR A., FLEISCHMANN D., WEGENKITTL R., GRÖLLER M. E.: Diagnostic relevant visualization of vascular structures. In *Proc. of Scientific Visualization: The Visual Extraction of Knowledge from Data. Mathematics and Visualization* (2006), Springer, pp. 207–228. 8, 9

[KHP08] KWON M. J., HAHN J., PARK H.: A fast spherical inflation method of the cerebral cortex by deformation of a simplex mesh on the polar coordinates. *International Journal of Imaging Systems and Technology 18*, 1 (2008), 9–16. 4, 16

[KLR*13] KLEMM P., LAWONN K., RAK M., PREIM B., TÖNNIES K. D., HEGENSCHEID K., VÖLZKE H., OELTZE S.: Visualization and analysis of lumbar spine canal variability in cohort study data. In *Proc. of Vision, Modeling and Visualization* (2013), pp. 121–128. 4, 21

[KMD*17] KHUNG S., MASSET P., DUHAMEL A., FAIVRE J.-B., FLOHR T., REMY J., REMY-JARDIN M.: Automated 3d rendering of ribs in 110 polytrauma patients: Strengths and limitations. *Academic Radiology 24*, 2 (2017), 146–152. 20

[KMP*15] KÖHLER B., MEUSCHKE M., PREIM U., FISCHBACH K., GUTBERLET M., PREIM B.: Two-dimensional plot visualization of aortic vortex flow in cardiac 4D PC-MRI data. In *Proc. of Bildverarbeitung für die Medizin* (2015), pp. 257–261. 4, 6

[KPS14] KRETSCHMER J., PREIM B., STAMMINGER M.: Bilateral Depth Filtering for Enhanced Vessel Reformation. In *EuroVis - Short Papers* (2014), Elmqvist N., Hlawitschka M., Kennedy J., (Eds.). 23

[KR16] KREISER J., ROPINSKI T.: Classifying medical projection techniques based on parameterization attribute preservation. In *EuroVis Workshop on Reproducibility, Verification, and Validation in Visualization (EuroRV3)* (2016), Lawonn K., Hlawitschka M., Rosenthal P., (Eds.), The Eurographics Association. 24

[KST*14] KRETSCHMER J., SOZA G., TIETJEN C., SUEHLING M., PREIM B., STAMMINGER M.: ADR – Anatomy-Driven Reformation. *IEEE Transactions on Visualization and Computer Graphics 20*, 12 (2014), 2496–2505. 4, 21, 22

[KSW06] KRUGER J., SCHNEIDER J., WESTERMANN R.: Clearview: An interactive context preserving hotspot visualization technique. *IEEE Transactions on Visualization and Computer Graphics 12*, 5 (2006). 24

[KSZ14] KHOSRAVI H., SOLTANIAN-ZADEH H.: Multi-surface quasi-isometric flattening of the cortex. In *Proc. of IEEE Symposium on Biomedical Imaging* (2014), pp. 1226–1229. 4, 18, 24

[KWF*01] KANITSAR A., WEGENKITTL R., FELKEL P., FLEISCHMANN D., SANDNER D., GRÖLLER M. E.: Computed tomography angiography: A case study of peripheral vessel investigation. In *Proc. of IEEE Visualization* (2001), pp. 477–480. 8

[KWFG03] KANITSAR A., WEGENKITTL R., FLEISCHMANN D., GRÖLLER M. E.: Advanced curved planar reformation: Flattening of vascular structures. In *Proc. of IEEE Visualization* (2003), pp. 43–50. 4, 9

[Lar01] LARSSON J.: *Imaging vision: functional mapping of intermediate visual processes in man*. Institutionen för neurovetenskap/Department of Neuroscience, 2001. 2

[LCMH09] LAMPE O. D., CORREA C., MA K.-L., HAUSER H.: Curve-centric volume reformation for comparative visualization. *IEEE Transactions on Visualization and Computer Graphics 15*, 6 (2009), 1235–1242. 4, 10, 11

[LGZ08] LV X., GAO X., ZOU H.: Interactive curved planar reformation based on snake model. *Computerized Medical Imaging and Graphics 32*, 8 (2008), 662–669. 4, 10

[LI15] LI X., IYENGAR S.: On computing mapping of 3d objects: A survey. *ACM Computing Surveys 47*, 2 (2015), 34. 2

[LLS05] LEE H.-J., LIM S., SHIN B.-S.: Unfolding of virtual endoscopy using ray-template. In *Proc. of Biological and Medical Data Analysis, Lecture Notes in Computer Science* (2005), vol. 3745, pp. 69–77. 4, 13

[LPRM02] LÉVY B., PETITJEAN S., RAY N., MAILLOT J.: Least squares conformal maps for automatic texture atlas generation. *ACM Transactions on Graphics 21*, 3 (2002), 362–371. 7, 16

[LR06] LEE N., RASCH M.: Tangential curved planar reformation for topological and orientation invariant visualization of vascular trees. In *Proc. of IEEE Engineering in Medicine and Biology Society* (2006), vol. 1, pp. 1073–1076. 4, 9

[LTW*10] LUI L. M., THIRUVENKADAM S., WANG Y., THOMPSON P. M., CHAN T. F.: Optimized conformal surface registration with shape-based landmark matching. *SIAM Journal on Imaging Sciences 3*, 1 (2010), 52–78. 4, 17

[LZ14] LU L., ZHAO J.: Virtual colon flattening method based on colonic outer surface. *Computer Methods and Programs in Biomedicine 117*, 3 (2014), 473–481. 4, 14

[MBS*10] MARKL M., BRENDECKE S., SIMON J., FRYDRYCHOWICZ A., HARLOFF A.: Coregistration of wall shear stress and plaque distribution within the thoracic aorta of acute stroke patients. *Magnetic Resonance in Medicine 18* (2010). 4, 6

[MC10] MCINERNEY T., CRAWFORD P.: Ribbonview: interactive context-preserving cutaways of anatomical surface meshes. In *Advances in Visual Computing*. Springer, 2010, pp. 533–544. 24

[MDB*11] MARINO J., DU W., BARISH M., LI E., ZHU W., KAUFMAN A.: Evaluation of electronic biopsy for clinical diagnosis in virtual colonoscopy. In *Proc. of SPIE Medical Imaging* (2011), vol. 7964, p. 796419. 4, 13

[MHS07] MAI Z., HUYSMANS T., SIJBERS J.: Colon visualization using cylindrical parameterization. In *Proc. of International Conference on Advanced Concepts for Intelligent Vision Systems* (2007), Springer, pp. 607–615. 4, 13

[Mis13] MISTELBAUER G.: *Smart Interactive Vessel Visualization in Radiology*. PhD thesis, Institute of Computer Graphics and Algorithms, TU Wien, Vienna, Austria, 2013. 11

[MK10] MARINO J., KAUFMAN A.: Colon visualization using shape preserving flattening. In *Proc. of MICCAI Workshop on Computational Challenges and Clinical Opportunities in Virtual Colonoscopy and Abdominal Imaging* (2010), pp. 120–125. 13

[MK16] MARINO J., KAUFMAN A.: Planar visualization of treelike structures. *IEEE Transactions on Visualization and Computer Graphics 22*, 1 (2016), 906–915. 4, 12, 24

[MKP*16] MEUSCHKE M., KÖHLER B., PREIM U., PREIM B., LAWONN K.: Semi-automatic vortex flow classification in 4D PC-MRI data of the aorta. *Computer Graphics Forum 35*, 3 (2016), 351–360. 4, 6

[MMK*17] MIAO H., MISTELBAUER G., KARIMOV A., ALANSARY A., DAVIDSON A., LLOYD D. F. A., DAMODARAM M., STORY L., HUTTER J., HAJNAL J. V., RUTHERFORD M., PREIM B., KAINZ B., GRÖLLER M. E.: Placenta maps: In utero placental health assessment of the human fetus. *IEEE Transactions on Visualization and Computer Graphics 23*, 6 (2017), 1612–1623. 4, 12, 23

[MMV*13] MISTELBAUER G., MORAR A., VARCHOLA A., SCHERNTHANER R., BACLIJA I., KÖCHL A., KANITSAR A., BRUCKNER S., GRÖLLER M. E.: Vessel Visualization using Curvicircular Feature Aggregation. *Computer Graphics Forum 32*, 3 (2013), 231–240. 4, 9, 11

[MPG*17] MARTINKE H., PETRY C., GROSSKOPF S., SUEHLING M., SOZA G., PREIM B., MISTELBAUER G.: Bone fracture and lesion assessment using shape-adaptive unfolding. In *Proc. of Eurographics Workshop on Visual Computing for Biology and Medicine* (2017), pp. 149–158. 4, 21, 22

[MST06] MEMOLI F., SAPIRO G., THOMPSON P.: Geometric surface and brain warping via geodesic minimizing lipschitz extensions. In *Proc. of MICCAI Workshop on Mathematical Foundations of Computational Anatomy: Geometrical, Statistical and Registration Methods for Modeling Biological Shape Variability* (2006), pp. 58–67. 4, 16

[MVB*12] MISTELBAUER G., VARCHOLA A., BOUZARI H., STARINSKY J., KÖCHL A., SCHERNTHANER R., FLEISCHMANN D., GRÖLLER M. E., ŠRÁMEK M.: Centerline reformations of complex vascular structures. In *Proc. of IEEE Pacific Visualization Symposium* (2012), pp. 233–240. 4, 10

[MVB*17] MEUSCHKE M., VOSS S., BEUING O., PREIM B., LAWONN K.: Combined visualization of vessel deformation and hemodynamics in cerebral aneurysms. *IEEE Transactions on Visualization and Computer Graphics 23*, 1 (2017), 761–770. 4, 7, 12

[MZGK11] MARINO J., ZENG W., GU X., KAUFMAN A.: Context preserving maps of tubular structures. *IEEE Transactions on Visualization and Computer Graphics 17*, 12 (2011), 1997–2004. 13

[NGB*09] NEUGEBAUER M., GASTEIGER R., BEUING O., DIEHL V., SKALEJ M., PREIM B.: Map displays for the analysis of scalar data on cerebral aneurysm surfaces. *Computer Graphics Forum 28*, 3 (2009), 895–902. 4, 7, 24

[NMGK17] NADEEM S., MARINO J., GU X., KAUFMAN A.: Corresponding supine and prone colon visualization using eigenfunction analysis and fold modeling. *IEEE Transactions on Visualization and Computer Graphics 23*, 1 (2017), 751–760. 4, 14

[OGH*06] OELTZE S., GROTHUES F., HENNEMUTH A., KUSS A., PREIM B.: Integrated visualization of morphologic and perfusion data for the analysis of coronary artery disease. In *Proc. of IEEE Eurographics Symposium on Visualization* (2006), pp. 131–138. 4, 5

[OJMN*18] OELTZE-JAFFRA S., MEUSCHKE M., NEUGEBAUER M., SAALFELD S., LAWONN K., JANIGA G., HEGE H.-C., ZACHOW S., PREIM B.: Generation and visual exploration of medical flow data: Survey, research trends, and future challenges. *Computer Graphics Forum* (2018), (to appear). 3

[PB13] PREIM B., BOTHA C. P.: *Visual computing for medicine: theory, algorithms, and applications*. Newnes, 2013. 2

[PKF04] PONS J.-P., KERIVEN R., FAUGERAS O.: Area preserving cortex unfolding. In *Proc. of Medical Image Computing and Computer-Assisted Intervention* (2004), pp. 376–383. 4, 16

[PSH*04] PORTUGALLER H. R., SCHOELLNAST H., HAUSEGGER K. A., TIESENHAUSEN K., AMANN W., BERGHOLD A.: Multislice spiral CT angiography in peripheral arterial occlusive disease: a valuable tool in detecting significant arterial lumen narrowing? *European Radiology 14*, 9 (2004), 1681–1687. 23

[RKSH11] RIEDER C., KROEGER T., SCHUMANN C., HAHN H. K.: GPU-based real-time approximation of the ablation zone for radiofrequency ablation. *IEEE transactions on visualization and computer graphics 17*, 12 (2011), 1812–1821. 23

[RLT*15] RINGL H., LAZAR M., TÖPKER M., WOITEK R., PROSCH H., ASENBAUM U., BALASSY C., TOTH D., WEBER M., HAJDU S., SOZA G., WIMMER A., MANG T.: The ribs unfolded - a CT visualization algorithm for fast detection of rib fractures: effect on sensitivity and specificity in trauma patients. *European Radiology 25*, 7 (2015), 1865–1874. 4, 20

[RSH06] ROPINSKI T., STEINICKE F., HINRICHS K.: Visually supporting depth perception in angiography imaging. In *Proc. of International Symposium on Smart Graphics* (2006), pp. 93–104. 20

[RSS*10] RINGL H., SCHERNTHANER R. E., SCHUELLER G., BALASSY C., KIENZL D., BOTOSANEANU A., WEBER M., CZERNY C., HAJDU S., MANG T., ET AL.: The skull unfolded: A cranial ct visualization algorithm for fast and easy detection of skull fractures. *Radiology 255*, 2 (2010), 553–562. 4, 22

[RWS*10] RIEDER C., WEIHUSEN A., SCHUMANN C., ZIDOWITZ S., PEITGEN H.-O.: Visual support for interactive post-interventional assessment of radiofrequency ablation therapy. *Computer Graphics Forum 29*, 3 (2010), 1093–1102. 4, 19, 20, 23

[Sar06] SAROUL L.: *Surface extraction and flattening for anatomical visualization*. PhD thesis, Université de Saint-Etienne, France, 2006. 2, 4, 20

[SCK*16] SHEHARYAR A., CHITIBOI T., KELLER E., RAHMAN O., SCHNELL S., MARKL M., BOUHALI O., LINSEN L.: Spatio-temporal Visualization of Regional Myocardial Velocities. In *Proc. of Eurographics Workshop on Visual Computing for Biology and Medicine* (2016), pp. 89–98. 4, 5

[SF04] STYLIANOU G., FARIN G.: Crest lines for surface segmentation and flattening. *IEEE Transactions on Visualization & Computer Graphics*, 5 (2004), 536–544. 4, 16

[SL02] SHATTUCK D. W., LEAHY R. M.: BrainSuite: an automated cortical surface identification tool. *Medical Image Analysis 6*, 2 (2002), 129–142. 2

[SMF*17] SIEGEL R. L., MILLER K. D., FEDEWA S. A., AHNEN D. J., MEESTER R. G., BARZI A., JEMAL A.: Colorectal cancer statistics, 2017. *CA: A Cancer Journal for Clinicians 67*, 3 (2017), 177–193. 12

[SPR06] SHEFFER A., PRAUN E., ROSE K.: Mesh parameterization methods and their applications. *Foundations and Trends® in Computer Graphics and Vision 2*, 2 (2006), 105–171. 2

[SSW89] SCHWARTZ E. L., SHAW A., WOLFSON E.: A numerical solution to the generalized mapmaker's problem: flattening nonconvex polyhedral surfaces. *IEEE Transactions on Pattern Analysis and Machine Intelligence 11*, 9 (1989), 1005–1008. 17

[ST90] SHIRLEY P., TUCHMAN A.: A polygonal approximation to direct scalar volume rendering. In *workshop on Volume visualization* (1990), pp. 63–70. 14

[SWM*15] SCHERNTHANER R. E., WOLF F., MISTELBAUER G., WEBER M., SRAMEK M., GROELLER E., LOEWE C.: New hybrid reformations of peripheral CT angiography: do we still need axial images? *Clinical imaging 39*, 4 (2015), 603–607. 23

[SZS*13] SU Z., ZENG W., SHI R., WANG Y., SUN J., GU X.: Area preserving brain mapping. In *Proc. of the IEEE Conference on Computer Vision and Pattern Recognition* (2013), pp. 2235–2242. 4, 18

[TBB*07] TERMEER M., BESCOS J. O., BREEUWER M., VILANOVA A., GERRITSEN F., GRÖLLER E.: CoViCAD: comprehensive visualization of coronary artery disease. *IEEE Transactions on Visualization and Computer Graphics 13*, 6 (2007), 1632–1639. 4, 5, 6, 23, 24

[THQ*16] TAO J., HUANG X., QIU F., WANG C., JIANG J., SHENE C.-K., ZHAO Y., YU D.: VesselMap: A web interface to explore multivariate vascular data. *Computers & Graphics 59* (2016), 79–92. 4, 7

[Tim99] TIMSARI B.: *Geometrical Modeling and Analysis of Cortical Surfaces: An Approach to Finding Flat Maps of The Human Brain*. PhD thesis, University of Southern California, Los Angeles, California, 1999. 4, 15

[TL00] TIMSARI B., LEAHY R. M.: Optimization method for creating semi-isometric flat maps of the cerebral cortex. In *Proc. of SPIE Medical Imaging* (2000), pp. 698–708. 4, 15

[TP01] TOSUN D., PRINCE J. L.: Hemispherical map for the human brain cortex. In *Proc. of SPIE Medical Imaging* (2001), pp. 290–300. 4, 16

[TRH*04] TOSUN D., RETTMANN M. E., HAN X., TAO X., XU C., RESNICK S. M., PHAM D. L., PRINCE J. L.: Cortical surface segmentation and mapping. *NeuroImage 23* (2004), 108–118. 4, 16

[TRP04] TOSUN D., RETTMANN M. E., PRINCE J. L.: Mapping techniques for aligning sulci across multiple brains. *Medical Image Analysis 8*, 3 (2004), 295–309. 4, 16

[TT99] TOGA A. W., THOMPSON P.: An introduction to brain warping. In *Proc. of Brain Warping* (1999), pp. 1–26. 2

[Tut60] TUTTE W. T.: Convex representations of graphs. *Proc. of London Mathematical Society 10*, 38 (1960), 304–320. 16

[Tut63] TUTTE W. T.: How to draw a graph. *Proc. of London Mathematical Society 13*, 3 (1963), 743–768. 16

[VED97] VAN ESSEN D., DRURY H.: Structural and functional analyses of human cerebral cortex using a surface-based atlas. *The Journal of Neuroscience 17*, 18 (1997), 7079–7102. 15

[VEDD*01] VAN ESSEN D. C., DRURY H. A., DICKSON J., HARWELL J., HANLON D., ANDERSON C. H.: An integrated software suite for surface-based analyses of cerebral cortex. *Journal of the American Medical Informatics Association 8*, 5 (2001), 443–459. 2

[VLP05] VRTOVEC T., LIKAR B., PERNUŠ F.: Automated curved planar reformation of 3D spine images. *Physics in Medicine & Biology 50* (2005), 4527–4540. 4, 20

[VOG*06] VRTOVEC T., OURSELIN S., GOMES L., LIKAR B., PERNUŠ F.: Generation of curved planar reformations from magnetic resonance images of the spine. In *Proc. of Medical Image Computing and Computer-Assisted Intervention* (2006), pp. 135–143. 4, 20

[VOG*07] VRTOVEC T., OURSELIN S., GOMES L., LIKAR B., PERNUŠ F.: Automated generation of curved planar reformations from MR images of the spine. *Physics in Medicine & Biology 52*, 10 (2007), 2865–2878. 4, 20

[Vrt15] VRTOVEC T.: Automated determination of the spine-based coordinate system for an efficient cross-sectional visualization of 3d spine images. In *Proc. of Spinal Imaging and Image Analysis* (2015), vol. 18, pp. 231–299. 20

[WCB00] WANDELL B. A., CHIAL S., BACKUS B. T.: Visualization and measurement of the cortical surface. *Journal of Cognitive Neuroscience 12*, 5 (2000), 739–752. 4, 15

[WGC*04a] WANG Y., GU X., CHAN T. F., THOMPSON P. M., YAU S.-T.: Intrinsic brain surface conformal mapping using a variational method. In *Proc. of SPIE Medical Imaging* (2004), pp. 241–252. 4, 16

[WGC*04b] WANG Y., GU X., CHAN T. F., THOMPSON P. M., YAU S.-T.: Volumetric harmonic brain mapping. In *Proc. of IEEE Symposium on Biomedical Imaging* (2004), pp. 1275–1278. 4, 16, 24

[WGC*08a] WANG Y., GU X., CHAN T. F., THOMPSON P. M., YAU S.-T.: Conformal slit mapping and its applications to brain surface parameterization. In *Proc. of Medical Image Computing and Computer-Assisted Intervention* (2008), pp. 585–593. 4, 17

[WGC*08b] WILLIAMS D., GRIMM S., COTO E., ROUDSARI A., HATZAKIS H.: Volumetric curved planar reformation for virtual endoscopy. *IEEE Transactions on Visualization and Computer Graphics 14*, 1 (2008), 109–119. 4, 13

[WLG*07] WANG Y., LUI L. M., GU X., HAYASHI K. M., CHAN T. F., TOGA A. W., THOMPSON P. M., YAU S.-T.: Brain surface conformal parameterization using riemann surface structure. *IEEE Transactions on Medical Imaging 26*, 6 (2007), 853–865. 17

[WSY*12] WANG Y., SHI J., YIN X., GU X., CHAN T. F., YAU S.-T., TOGA A. W., THOMPSON P. M.: Brain surface conformal parameterization with the ricci flow. *IEEE Transactions on Medical Imaging 31*, 2 (2012), 251–264. 4, 17, 18

[WZG*10] WANG Y., ZHANG J., GUTMAN B., CHAN T. F., BECKER J. T., AIZENSTEIN H. J., LOPEZ O. L., TAMBURO R. J., TOGA A. W., THOMPSON P. M.: Multivariate tensor-based morphometry on surfaces: application to mapping ventricular abnormalities in HIV/AIDS. *NeuroImage 49*, 3 (2010), 2141–2157. 19

[ZHGH11] ZOU G., HU J., GU X., HUA J.: Area-preserving surface flattening using lie advection. In *Proc. of Medical Image Computing and Computer-Assisted Intervention* (2011), pp. 335–342. 4, 17, 18, 23

[ZHT*02a] ZHU L., HAKER S., TANNENBAUM A., BOUIX S., SIDDIQI K.: Angle-preserving mappings for the visualization of multi-branched vessels. In *Proc. of the International Conference on Image Processing* (2002), vol. 2, pp. 945–948. 4, 9

[ZHT02b] ZHU L., HAKER S., TANNENBAUM A. R.: Conformal flattening maps for the visualization of vessels. In *Proc. of SPIE Medical Imaging: Visualization, Image-Guided Procedures, and Display* (2002), vol. 4681, pp. 742–748. 4, 9

[ZHT03] ZHU L., HAKER S., TANNENBAUM A.: Area-preserving mappings for the visualization of medical structures. In *Proc. of Medical Image Computing and Computer-Assisted Intervention* (2003), pp. 277–284. 4, 9

[ZHT05] ZHU L., HAKER S., TANNENBAUM A.: Flattening maps for the visualization of multibranched vessels. *IEEE Transactions on Medical Imaging 24*, 2 (2005), 191–198. 4, 9, 10

[ZMG*10] ZENG W., MARINO J., GURIJALA K. C., GU X., KAUFMAN A.: Supine and prone colon registration using quasi-conformal mapping. *IEEE Transactions on Visualization and Computer Graphics 16*, 6 (2010), 1348–1357. 4, 13, 14

[ZMGK10] ZENG W., MARINO J., GU X., KAUFMAN A.: Conformal geometry based supine and prone colon registration. In *Proc. of MICCAI Workshop on Computational Challenges and Clinical Opportunities in Virtual Colonoscopy and Abdominal Imaging* (2010), pp. 113–119. 4, 13

[ZMKG11] ZENG W., MARINO J., KAUFMAN A., GU X. D.: Volumetric colon wall unfolding using harmonic differentials. *Computers & Graphics 35*, 3 (2011), 726–732. 4, 14, 24

[ZYHT07] ZHU L., YANG Y., HAKER S., TANNENBAUM A.: An image morphing technique based on optimal mass preserving mapping. *Image Processing, IEEE Transactions on 16*, 6 (2007), 1481–1495. 24